

Original Research

Predicting critical drug concentrations and torsadogenic risk using a multiscale exposure-response simulator

Francisco Sahli Costabal ^a, Jiang Yao ^b, Anna Sher ^c, Ellen Kuhl ^{a,*}^a Department of Mechanical Engineering, Stanford University, Stanford, CA, 94305, United States^b Dassault Systèmes Simulia Corporation, Johnston, RI, 02919, United States^c Internal Medicine Research Unit, Pfizer Inc, Cambridge, MA, 02139, United States

ARTICLE INFO

Article history:

Received 1 March 2018

Received in revised form

21 September 2018

Accepted 11 October 2018

Available online 26 October 2018

Keywords:

Electrophysiology

Pharmacology

Torsades de pointes

Early afterdepolarizations

Computational modeling

Finite element analysis

ABSTRACT

Torsades de pointes is a serious side effect of many drugs that can trigger sudden cardiac death, even in patients with structurally normal hearts. Torsadogenic risk has traditionally been correlated with the blockage of a specific potassium channel and a prolonged recovery period in the electrocardiogram. However, the precise mechanisms by which single channel block translates into heart rhythm disorders remain incompletely understood. Here we establish a multiscale exposure-response simulator that converts block-concentration characteristics from single cell recordings into three-dimensional excitation profiles and electrocardiograms to rapidly assess torsadogenic risk. For the drug dofetilide, we characterize the QT interval and heart rate at different drug concentrations and identify the critical concentration at the onset of torsades de pointes: For dofetilide concentrations of 2x, 3x, and 4x, as multiples of the free plasma concentration $C^{\max} = 2.1 \text{ nM}$, the QT interval increased by +62.0%, +71.2%, and +82.3% compared to baseline, and the heart rate changed by -21.7%, -23.3%, and +88.3%. The last number indicates that, at the critical concentration of 4x, the heart spontaneously developed an episode of a torsades-like arrhythmia. Strikingly, this critical drug concentration is higher than the concentration estimated from early afterdepolarizations in single cells and lower than in one-dimensional cable models. Our results highlight the importance of whole heart modeling and explain, at least in part, why current regulatory paradigms often fail to accurately quantify the pro-arrhythmic potential of a drug. Our exposure-response simulator could provide a more mechanistic assessment of pro-arrhythmic risk and help establish science-based guidelines to reduce rhythm disorders, design safer drugs, and accelerate drug development.

© 2018 Elsevier Ltd. All rights reserved.

1. Introduction

The average cost to develop a new drug is \$2.5 billion (DiMasi et al., 2016) and the time to market is more than ten years (DiMasi et al., 2003). A critical step in the approval of any new drug is the assessment of its side effects on the heart (Colatsky et al., 2016). Numerous drugs, not just cardiac drugs, are known to interact with specific ionic channels and induce potentially lethal cardiac arrhythmias (Crumb et al., 2016). While there is a general agreement that pro-arrhythmic risk evaluation is critical to avoid the introduction of potentially dangerous drugs to the market (Navarrete et al., 2013), the high cost and long time to test new

compounds often hinders the discovery of new drugs. The current gold standard to assess the pro-arrhythmic risk of a drug is to measure its effects on a specific potassium current in single cell experiments (Redfern et al., 2003) and on the QT interval in the electrocardiogram (Gintant et al., 2016). However, not all the drugs that fail these tests actually cause arrhythmias: Many safe and potentially useful drugs are screened out of the early stages of development because of the poor specificity of the current biomarkers for cardiac toxicity (Stockbridge et al., 2013). A better mechanistic understanding of drug-induced arrhythmias is therefore critical to more reliably predict cardiac toxicity and accelerate drug development.

Drugs that are classified to have a high pro-arrhythmic potential typically have one thing in common: They interact with a voltage-gated potassium channel encoded by the human *ether-à-go-go* related gene hERG (Trudeau et al., 1995). To no surprise, hERG

* Corresponding author.

E-mail address: ekuhl@stanford.edu (E. Kuhl).

inhibition is routinely screened for in new drugs (Johannesen et al., 2014). On the ion channel level, blocking the hERG channel reduces the delayed rectifier potassium current I_{Kr} , which slows down the flux of positively charged potassium ions out of the cell (Wang and MacKinnon, 2017). On the cellular level, this reduces the repolarization rate (Fink et al., 2008), increases the refractory period, and widens the plateau of the action potential (Mirams et al., 2011). On the whole heart level, this delay induces a prolongation of the QT interval, a signature that is associated with a high risk of torsades de pointes (Bohnen et al., 2017). Torsades de pointes is a polymorphic ventricular tachycardia characterized by rapid, irregular QRS complexes that twist around the electrocardiogram baseline (Dessertenne, 1966). Most episodes of torsades de pointes begin spontaneously and revert to normal sinus rhythm within a few seconds, but some persist, degenerate into ventricular fibrillation, and lead to sudden cardiac death.

In the United States, 300,000 sudden cardiac deaths occur each year, but the true incidence of torsades de pointes is largely unknown. The reporting rate of torsades de pointes increased exponentially in the early 1990s when numerous drugs were recognized to trigger QT interval prolongation and increase pro-arrhythmic risk (Stockbridge et al., 2013). In response, 14 drugs were removed from the market, amongst them dofetilide, a class III anti-arrhythmic agent that cardioverts persistent atrial fibrillation into regular sinus rhythm (Lenz and Hilleman, 2000). Despite its favorable risk-to-benefit profile, dofetilide remains a controversial drug (Abraham et al., 2015). While it is still unavailable in Europe and Australia, in the United States, it is available in three doses, 0.125 mg, 0.250 mg, and 0.500 mg (Pfizer, 2011). Studies have shown that increasing the dose of dofetilide increases the degree of potassium channel block and with it the risk of torsades de pointes (Crumb et al., 2016). Although a mandatory risk management program has been established to tightly regulate the usage and dosage of dofetilide (Allen LaPointe et al., 2003), the incidence of dofetilide-induced torsades de pointes is high and drug mismanagement is a significant problem (Briceno and Supple, 2017).

The precise mechanisms by which drugs like dofetilide trigger the initiation of cardiac arrhythmias remain insufficiently understood (Macdonald et al., 2018). Increasing evidence suggests that early afterdepolarizations play a critical role in inducing torsadogenesis (Qu et al., 2013). Early afterdepolarizations are oscillations during the repolarization phase of the action potential that result from a reduced outward current, an increased inward current, or both (Roden et al., 1996). On the cellular level, endogenous membrane currents alone determine whether or not early afterdepolarizations occur. On the tissue level, however, early afterdepolarizations are a result of the interplay of endogenous currents and exogenous currents from neighboring cells (Weiss et al., 2010). In cardiac electrophysiology this condition is known as source-sink mismatch. It implies that a sufficient number of neighboring cells have to exhibit early afterdepolarizations to generate a strong enough effect to propagate into the surrounding tissue (Sato et al., 2009). However, the precise number of required afterdepolarizing cells, and with it the critical condition for torsades de pointes, is not entirely clear (Xie et al., 2010).

Researchers, the pharmaceutical industry, and regulatory agencies are beginning to recognize the significance of drug-induced arrhythmias and have started to join forces towards developing and validating new paradigms for cardiac safety evaluation (Colatsky et al., 2016). A promising initiative is the Comprehensive in-vitro Proarrhythmia Assay CiPA lead by the Food and Drug Administration to establish new mechanistic assays that can predict the pro-arrhythmic risk of new compounds (Sager et al., 2014). One of the main recommendations of the CiPA initiative is to promote computational modeling (Chabiniok et al., 2016) to

characterize the effect of drugs (Vicente et al., 2016). The long-term vision is that mechanistic modeling will allow us to quickly screen new compounds and estimate their torsadogenic risk (Vicente et al., 2018). First efforts are underway to risk-stratify common drugs using single cell models (Mirams et al., 2011; Lancaster and Sobie, 2016; Abbasi et al., 2017; Krogh-Madsen et al., 2017; Parikh et al., 2017; Passini et al., 2017), one-dimensional cable models (Beattie et al., 2013), and three-dimensional models (Okada et al., 2015). Only very recently have researchers begun to integrate the knowledge from single cell modeling, one-dimensional modeling, and three-dimensional modeling in a single unified biomarker for cardiac arrhythmias (Dutta et al., 2016).

Motivated by these open questions, we have created a mechanistic exposure-response simulator to predict how drug-induced current block on the ion channel level translates into action potential profiles on the single cell level and into electrocardiograms on the whole heart level (Sahli Costabal et al., 2018a, 2018b). Our simulations allow us to identify the critical drug concentration at which early afterdepolarizations occur within a cell and at which torsades de pointes develops across the whole heart. We will demonstrate that these critical drug concentrations do not necessarily coincide. Our results suggest that tissue heterogeneity plays a critical role in converting early afterdepolarizations on the cellular level into torsades de pointes on the whole heart level.

2. Methods

2.1. Modeling cardiac electrophysiology

We follow our established approach (Sahli Costabal et al., 2018a, 2018b) and model cardiac electrophysiology using the classical monodomain model to characterize the spatio-temporal evolution of the transmembrane potential ϕ ,

$$\dot{\phi} = \text{div}(\mathbf{D} \cdot \nabla \phi) + f^\phi. \quad (1)$$

For the flux term, $\text{div}(\mathbf{D} \cdot \nabla \phi)$, we assume an anisotropic conductivity \mathbf{D} with a fast signal propagation D^{\parallel} parallel to the fiber direction \mathbf{f} and a slow signal propagation D^{\perp} perpendicular to it (Sahli Costabal et al., 2017),

$$\mathbf{D} = D^{\parallel} \mathbf{f} \otimes \mathbf{f} + D^{\perp} [\mathbf{I} - \mathbf{f} \otimes \mathbf{f}], \quad (2)$$

where \mathbf{I} is the identity tensor and \otimes is the outer product. For the source term, $f^\phi = -I_{\text{ion}}/C_m$, we scale the ionic current I_{ion} by the membrane capacitance C_m (Nordsletten et al., 2011), and adopt different ionic models for the different cell types in the heart. In general, the ionic current is a function of the transmembrane potential ϕ and a set of state variables \mathbf{q} (Göktepe et al., 2010),

$$I_{\text{ion}} = I_{\text{ion}}(\phi, \mathbf{q}(\phi); t). \quad (3)$$

The state variables obey ordinary differential equations as functions of the transmembrane potential ϕ and their current values \mathbf{q} .

$$\dot{\mathbf{q}} = \mathbf{g}(\phi, \mathbf{q}(\phi); t). \quad (4)$$

The number of ionic currents I_{ion} and state variables \mathbf{q} determines the complexity of the model (Fink et al., 2011). Here we select different cell models for ventricular cells and Purkinje cells.

To model the cells in the ventricular wall, we adopt the O'Hara-Rudy model for human ventricular cardiomyocytes (O'Hara et al., 2011a). Fig. 1, left, illustrates the 15 ionic currents of the O'Hara-Rudy model,

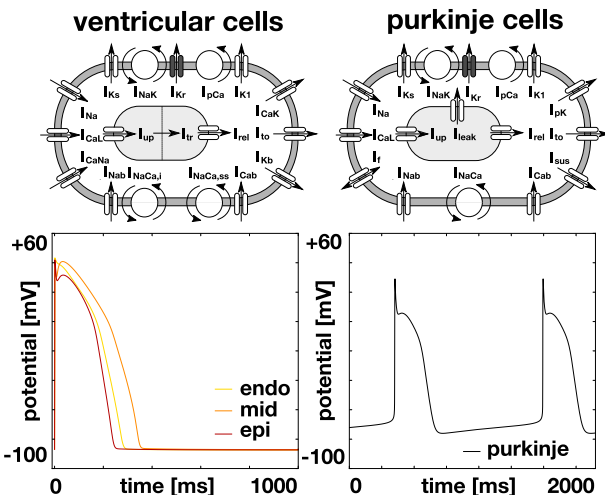


Fig. 1. Modeling cardiac electrophysiology. Cell models for human ventricular cardiomyocytes, left, and Purkinje fiber cells, right (Sahli Costabal et al., 2018a, 2018b). The ventricular cell model distinguishes between endocardial, midwall, and epicardial cells and is based on the modified O'Hara Rudy model with 15 ionic currents and 39 state variables (O'Hara et al., 2011a). The Purkinje cell model displays inherent automaticity and is based on the Stewart model with 14 ionic currents and 20 state variables (Stewart et al., 2009a).

$$\begin{aligned} I_{ion} = & I_{Kr} + I_{Ks} + I_{K1} + I_{CaL} \\ & + I_{Na} + I_{CaNa} + I_{CaK} + I_{Cab} + I_{Nab} + I_{Kb} \\ & + I_{to} + I_{NaK} + I_{pCa} + I_{NaCa,i} + I_{NaCa,ss}, \end{aligned} \quad (5)$$

the rapid and slow delayed rectifier potassium currents I_{Kr} and I_{Ks} , the inward rectifier potassium current I_{K1} , the L-type calcium current I_{CaL} , the fast and late sodium currents I_{Na} , the calcium sodium and calcium potassium currents I_{CaNa} and I_{CaK} , the background calcium, sodium, and potassium currents I_{Cab} , I_{Nab} , and I_{Kb} , the transient outward potassium current I_{to} , the sodium potassium pump current I_{NaK} , the sarcolemmal calcium pump current I_{pCa} , and the sodium calcium exchange currents $I_{NaCa,i}$ and $I_{NaCa,ss}$. To accurately model signal propagation in whole heart simulations (Priest et al., 2016), we replace the fast sodium current I_{Na} of the original O'Hara-Rudy model (O'Hara et al., 2011a) with the fast sodium current of the ten Tusscher model (ten Tusscher et al., 2004). The 15 currents are defined through a total of 39 state variables. To account for regional specificity, the O'Hara-Rudy model is parameterized for three different cell types, endocardial, midwall, and epicardial cells (O'Hara et al., 2011a). Fig. 1, left, illustrates the single cell action potential of the O'Hara-Rudy model for endocardial, mid, and epicardial human ventricular cardiomyocytes and Fig. 2 shows the distribution of these three cell types across the ventricular wall.

To model cells of the Purkinje fiber network, we choose the Stewart model for human Purkinje fiber cells (Stewart et al., 2009a). A distinguishing feature of this model is its automaticity, which enables the cells to self-excite without an external stimulus. Fig. 1, right, illustrates the 14 ionic currents of the Stewart model,

$$\begin{aligned} I_{ion} = & I_{Kr} + I_{Ks} + I_{K1} + I_{CaL} + I_{Na} + I_{Cab} + I_{Nab} \\ & + I_{to} + I_f + I_{sus} + I_{NaK} + I_{pCa} + I_{pK} + I_{NaCa}, \end{aligned} \quad (6)$$

the rapid and slow delayed rectifier potassium currents I_{Kr} and I_{Ks} , the inward rectifier potassium current I_{K1} , the L-type calcium current I_{CaL} , the fast and late sodium currents I_{Na} , the background calcium and sodium currents I_{Cab} and I_{Nab} , the transient outward potassium current I_{to} , the hyperpolarization-activated current I_f , the sustained potassium current I_{sus} , the sodium potassium pump

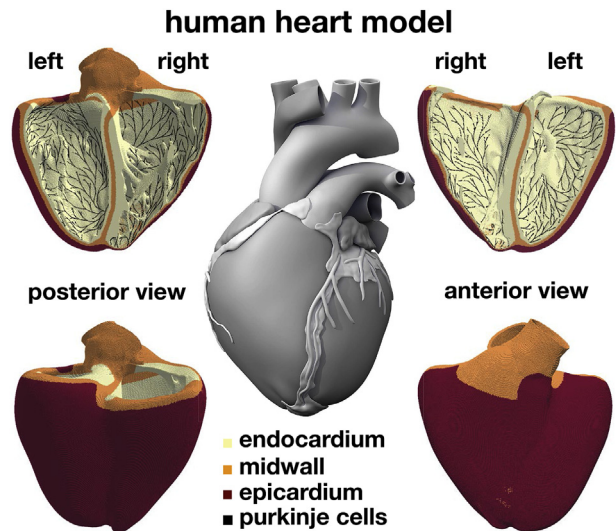


Fig. 2. Modeling the human heart. Anatomic model created from high resolution magnetic resonance images of a healthy male adult (Zygote Media Group, 2014) and finite element discretization (Sahli Costabal et al., 2018). The ventricular wall is discretized with 6,878,459 regular linear hexagonal finite elements with an edge length of 0.3 mm, a total number of 7,519,918 nodes, and 268,259,901 internal variables. The Purkinje fiber network is discretized with 39,772 linear cable elements, a total number of 39,842 nodes, and 795,440 internal variables. It is connected to the ventricles at its terminals through 3545 resistor elements. Endocardial, midwall, and epicardial cells are marked in yellow, orange, and red; Purkinje cells are shown in black (Sahli Costabal et al., 2016a).

current I_{NaK} , the calcium and potassium pump currents I_{pCa} and I_{pK} , and the sodium calcium exchange current I_{NaCa} . The 14 currents are defined through 20 state variables. Fig. 1, right, illustrates the single cell action potential for human Purkinje cells and Fig. 2 shows the Purkinje fiber network of our human heart model (Sahli Costabal et al., 2016a).

2.2. Modeling single cells

To solve the local problem of cardiac electrophysiology at the single cell level, we translate the original source codes for the O'Hara-Rudy model (O'Hara et al., 2011b) and for the Stewart model (Stewart et al., 2009b) into FORTRAN and adapt an explicit time integration scheme. For the ventricular cells, we pace the cells for 600 cycles at a rate of 60 beats per minute using the stimulus and time stepping scheme from the original model. For the Purkinje cells, we run the simulation for 120,000 ms and let the model self-excite. For both cases, we record and report the last 5000 ms.

2.3. Modeling cardiac tissue

To study how different cell types interact in the presence of drugs, we consider a simple cable model. We discretize a one-dimensional version of the set of continuum equations (1)–(5) in space and time using finite differences and adopt an explicit time integrator using our in-house code (Sahli Costabal et al., 2018c). The cable model is 1 cm long, similar to a transmural section of the ventricular wall, and is discretized with 100 elements of 100 μ m length, similar to the length of a healthy adult cardiac myocyte. The cable is composed of endocardial, midwall, and epicardial cells and has a conductivity of 0.13 mm^2/ms . We gradually vary the fraction of midwall cells from 30% to 90% in increments of 10%, and reduce the fraction of endocardial and epicardial cells accordingly from 35% to 5% each. To pace the cable, we apply a current to excite the first endocardial cell at a frequency of 60 beats per minute, similar

to the frequency of our Purkinje network, for a total of 30 beats. We record and report the action potential at a mid-wall cell in the center of the cable.

2.4. Modeling the human heart

To model cardiac electrophysiology across the human heart, we discretize the set of continuum equations (1)–(6) in space using finite elements and in time using finite differences (Sahli Costabal et al., 2018a). To solve the resulting system of equations, we adopt the finite element software package Abaqus (Dassault Systèmes, 2017). We capitalize on the structural similarity between cardiac electrophysiology and the classical heat transfer problem and adopt finite elements for heat transfer with a non-linear heat source. We discretize the transmembrane potential ϕ as a global degree of freedom at the node point level and the ionic currents I_{ion} and gating variables \mathbf{q} as internal variables on the integration point level (Göktepe and Kuhl, 2009). Inspired by the small time step size to resolve the sharp upstroke of the action potential, we adopt an explicit time integration scheme. Specifically, to solve the non-linear diffusion problem, we use the Abaqus 2017 double precision solver with default parameters and a fixed time step of 0.005 ms (Dassault Systèmes, 2017).

Fig. 2 illustrates our human heart model created from magnetic resonance images of a healthy, 21-year-old, 50th percentile U.S. male (Zygote Media Group, 2014). Motivated by the relation between element size and critical time step size in explicit methods, we convert the initial tetrahedral discretization (Baillargeon et al., 2014) into a regular discretization of cube elements with a constant edge length of 0.3 mm across the entire heart (Sahli Costabal et al., 2018a). This results in a discretization with a total of 6,878,459 regular linear hexagonal finite elements, 7,519,918 nodes, and 268,259,901 internal variables. For the flux term, we assume a faster conduction along the fiber direction \mathbf{f} (Baillargeon et al., 2014) with the conductivities parallel and perpendicular to the fiber direction as $D^{\parallel} = 0.090 \text{ mm}^2/\text{ms}$ and $D^{\perp} = 0.012 \text{ mm}^2/\text{ms}$ (Niederer et al., 1954). For the source term, we employ a body flux subroutine to incorporate the ionic currents I_{ion} in the finite element formulation (Dassault Systèmes, 2017). To account for the different cell types in the ventricular wall, we simulate a series of Laplace problems (Wong and Kuhl, 2010) and use our finite element mesh with different essential boundary conditions (Perotti et al., 2015). Motivated by the original O'Hara Rudy model, we do not model potential discrete islands of midwall cells (Nattel et al., 2011), but only account for transmural heterogeneity. Fig. 2 shows the resulting cell distribution with 20% endocardial cells, 30% midwall cells, and 50% epicardial cells marked in yellow, orange, and red. This arrangement ensures positive T-waves to simulate the healthy baseline electrocardiogram (Okada et al., 2011).

Fig. 2 shows our finite element model of the Purkinje fibers as a dense black network covering the endocardial surface. The Purkinje network is a critical ingredient to accurately model cardiac excitation and drive a regular baseline beat. We generate the Purkinje network as a fractal tree that grows on the endocardial surface of the left and right ventricles (Sahli Costabal et al., 2016a) using our freely available open source code (Sahli Costabal et al., 2016b). This results in a discretization with 39,772 linear cable elements, 39,842 nodes, and 795,440 internal variables (Sahli Costabal et al., 2018a). For these Purkinje elements, we implement a user element with a discrete one-dimensional version of equations (1)–(6). At the terminals of the fractal tree, we connect the Purkinje network to the neighboring myocardium. At these points, we use 3545 resistor

elements with a resistance of $1.78 \Omega\text{m}$ (Niederer et al., 1954; Bordas et al., 2012) to connect each endpoint of the network to the closest node of the ventricular mesh. This arrangement allows us to model a bi-directional conduction between the Purkinje network and the myocardium. For the Purkinje flux term, we choose a conductivity of $D^{\parallel} = 3.0 \text{ mm}^2/\text{ms}$ (Sahli Costabal et al., 2018a). A typical simulation of 5000 ms takes 37 h using 144 CPU cores on the Comet supercomputer (Towns et al., 2014).

To explore how the single-cell action potentials from Fig. 1 translate into the excitation profile of the entire heart, we excite the heart through the automaticity of the Purkinje network and post-process the resulting transmembrane potential profile to calculate pseudo electrocardiograms (Kotikanyadanam et al., 2010). At every point of the heart, we project the gradient of the transmembrane potential, $\nabla\phi$, onto the direction vector, $\nabla(1/\|\mathbf{r}\|)$, and integrate this projection across the entire cardiac domain,

$$\phi_e(\mathbf{x}_e) = - \int_{\mathcal{B}} \nabla\phi \cdot \nabla(1/\|\mathbf{r}\|) \, dV \quad \text{with} \quad \mathbf{r} = \mathbf{x}_e - \mathbf{x}. \quad (7)$$

The vector \mathbf{r} points from current point \mathbf{x} to the position of the virtual electrode \mathbf{x}_e (Sahli Costabal et al., 2018a). To model a precordial lead in the clinical electrocardiogram, we select an electrode position \mathbf{x}_e 2 cm away from the left ventricular wall. While the precise location of the electrode does modulate the amplitude of the electrocardiogram, it does not affect the pro-arrhythmic risk assessment of our study.

2.5. Modeling the effect of drugs

We model the effect of drugs on the single cell action potential by selectively blocking the relevant ionic currents as we have previously shown (Sahli Costabal et al., 2018a, 2018b). We adopt fractional block measurements for different concentrations from patch clamp electrophysiology (Crumb et al., 2016). To estimate the fractional block β at arbitrary concentrations C , we fit a Hill-type equation to the discrete measurement points,

$$\beta = \frac{C^h}{IC_{50}^h + C^h}. \quad (8)$$

The Hill-type equation has two parameters, the exponent h and the concentration IC_{50} required to achieve a 50% current block. Fig. 3 illustrates the effect of dofetilide, a selective blocker of the rapid delayed rectifier potassium current I_{Kr} . The graph highlights the fractional potassium current block β for varying concentrations C , log-normalized with respect to the free plasma concentration of dofetilide, $C^{\max} = 2.1 \text{ nM}$ (Crumb et al., 2016). The dots and error bars summarize the experimentally measured fractional blockage (Crumb et al., 2016) and the curve represents the fitted Hill model with $h = 0.65$ and $IC_{50} = 1.55 \text{ nM}$, highlighted as solid line. To apply the drug, we select a desired concentration C , calculate the fractional blockage β , and scale the rapid delayed rectifier potassium current,

$$I_{\text{Kr}}^{\text{drug}} = [1 - \beta] I_{\text{Kr}}, \quad (9)$$

by multiplying the baseline current I_{Kr} with the fractional blockage $[1 - \beta]$. We focus in particular on applying dofetilide at 2x, 3x, and 4x its free plasma concentration, $C^{\max} = 2.1 \text{ nM}$, corresponding to dofetilide concentrations of 4.08 nM , 5.83 nM , and 8.63 nM and blocking the rapid delayed rectifier potassium current I_{Kr} at 65%, 70%, and 75%.

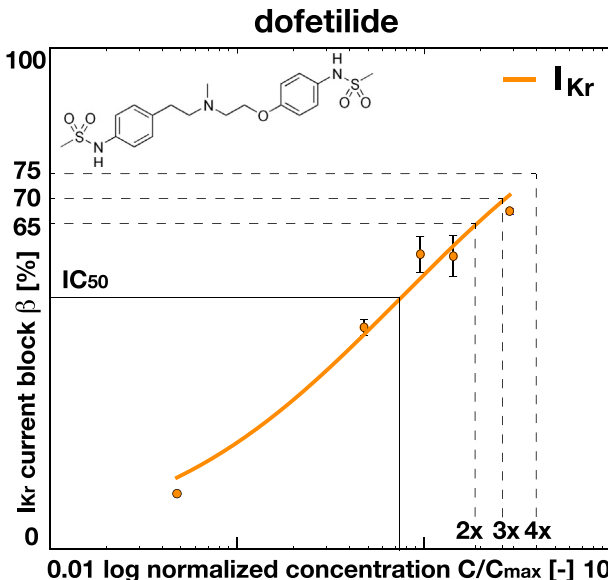


Fig. 3. Modeling the effect of drugs. Dofetilide selectively blocks the rapid delayed rectifier potassium current I_{Kr} . The degree of block β increases with increasing drug concentration C . The concentration is log-normalized with respect to the free plasma concentration of dofetilide, $C^{\max} = 2.1$ nM. Dots and error bars represent the mean and standard deviation of the experimentally measured fractional blockage (Crumb et al., 2016); the curve represents the fitted Hill model, $\beta = C^h / [IC_{50}^h + C^h]$, with $h = 0.65$ and $IC_{50} = 1.55$ nM, highlighted as solid line; the dotted lines represent an I_{Kr} current block of 65%, 70%, and 75% at dofetilide concentrations of 2x, 3x, and 4x of its free plasma concentration of $C^{\max} = 2.1$ nM (Sahli Costabal et al., 2018b).

3. Results

3.1. Midwall cells show early afterdepolarizations at 70% I_{Kr} block

Figs. 4 and 5 illustrate the effect of dofetilide on the single cell action potential ϕ , the ionic currents I_K , I_{Ca} , and I_{Na} , and the ion concentrations c_K , c_{Ca} , and c_{Na} in ventricular midwall cells using the single cell model from Section 2.2. Black lines represent the baseline potential, currents, and concentrations without the drug, yellow to red lines represent the modified potential, currents, and concentrations at a potassium channel block varying from $\beta = 10\%$ to 70% in increments of 10% . According to Fig. 3 and equation (8), $\beta = C^{0.65} / [1.55nM^{0.65} + C^{0.65}]$, these blocks correspond to dofetilide concentrations, $C = [\beta / (1 - \beta)]^{1/0.65} 1.55$ nM, varying from $C = 0.05$ nM to 5.83 nM. Blocking the potassium current I_{Kr} with dofetilide prolongs the plateau of the action potential and increases the overall action potential duration. Increasing the drug concentration, and with it the current block, increases this effect, from yellow to red. The single cell action potential profiles in Figs. 4 and 5 reveal the critical dofetilide concentration at which midwall cells begin to display early afterdepolarizations: Beyond a critical dofetilide concentration of $C = 5.83$ nM, at a potassium current block of 70% , midwall cells experience early afterdepolarizations and become self-oscillatory in every other beat, dark red curves. These oscillations are triggered by spikes in the L-type calcium current I_{CaL} , which can be observed in Fig. 4 and are also reflected in the intracellular calcium concentration c_{CaI} in Fig. 5. These single-cell profiles raise the question how midwall cells behave when they are surrounded by endocardial and epicardial cells.

3.2. Endo- and epicardial cells stabilize midwall cells and delay early afterdepolarizations beyond 70% I_{Kr} block

Fig. 6 summarizes the effect of blocking the rapid delayed

rectifier potassium current I_{Kr} at 65% , 70% , and 75% , which corresponds to dofetilide concentrations of 4.08 nM, 5.83 nM, and 8.63 nM, or, equivalently, $2x$, $3x$, and $4x$ the free plasma concentration of dofetilide. In contrast to Figs. 4 and 5, which display the effect of the drug on midwall cells in isolation, Fig. 6 highlights the effect of tissue heterogeneity in our one-dimensional model system of endocardial, midwall, and epicardial cells using the one-dimensional cardiac tissue model from Section 2.3. Black lines represent a model with 30% midwall cells, comparable to the midwall cell fraction in our whole heart model in Fig. 2. Yellow to red lines represent a gradual increase in midwall cells from 40% to 90% . Interestingly, the likelihood of early afterdepolarizations increases with increasing dofetilide concentration, from top to bottom, but decreases in the presence of endocardial and epicardial cells, from red to yellow. While midwall cells in isolation, in Figs. 4 and 5, display early afterdepolarizations beyond a critical block of 70% , embedded in a one-dimensional cable model, the critical block increases with increasing fractions of stabilizing endocardial and epicardial cells: At 65% block, none of the models displays early afterdepolarizations; at 70% block, only the model with 90% midwall cells displays early afterdepolarizations; and at 75% block, the models with $60\%-90\%$ midwall cells display early afterdepolarizations, while the models with $30\%-50\%$ midwall cells remain displaying single regular beats. Interestingly, the models with 60% and 70% midwall cells, shown in orange, alternate between sporadic early afterdepolarizations and regular beats, whereas the models with 80% and 90% midwall cells, shown in red, display oscillations in every beat at frequencies of 168 and 180 beats per minute. For our 1 cm-long model system, discretized with one hundred $100\mu\text{m}$ -long elements, these percentage numbers correspond roughly to the absolute number of required midwall cells, 90 for 70% block and 60 for 75% block. In view of this simple model study, we ask ourselves how the critical block of 70% and 75% of the one-dimensional cable model translates into the whole heart model.

3.3. Heterogeneity induces locally varying action potential profiles

Fig. 7 illustrates the effect of drugs using the whole heart model from Section 2.4. The center figure displays a characteristic snapshot of the transmembrane potential ϕ for a 75% potassium channel block corresponding to a dofetilide concentration of $4x$. The surrounding eight graphs highlight the heterogeneity of the cellular action potential at eight specific locations. Most cells display a small diastolic interval. Several cells display early afterdepolarizations. We did not observe marked delayed afterdepolarizations. Next, we study how these regionally varying local action potential profiles translate into the overall electrocardiogram.

3.4. Purkinje cells drive smooth, regular excitation at baseline

Fig. 8 displays the evolution of the transmembrane potential ϕ , representative potassium currents I_{Kr} , I_{Ks} , and I_{K1} , and the calcium current I_{CaL} for the baseline simulation with no drugs. The red graph shows the electrocardiogram, post-processed from the activation profile using equation (7). The black arrows indicate the ten time points associated with the ten columns. The electrocardiogram displays a regular periodic activation pattern at a heart rate of 60 beats per minute determined by the automaticity of the Purkinje fiber network. The length of the baseline QT interval is 271 ms. During depolarization, the Purkinje network drives the excitation from apex to base with a sharp depolarization front that propagates smoothly across the heart, columns 1 to 2. During repolarization, both ventricles gradually return to their resting state, columns 3 to 6. The excitation pattern repeats itself identically every 1000 ms,

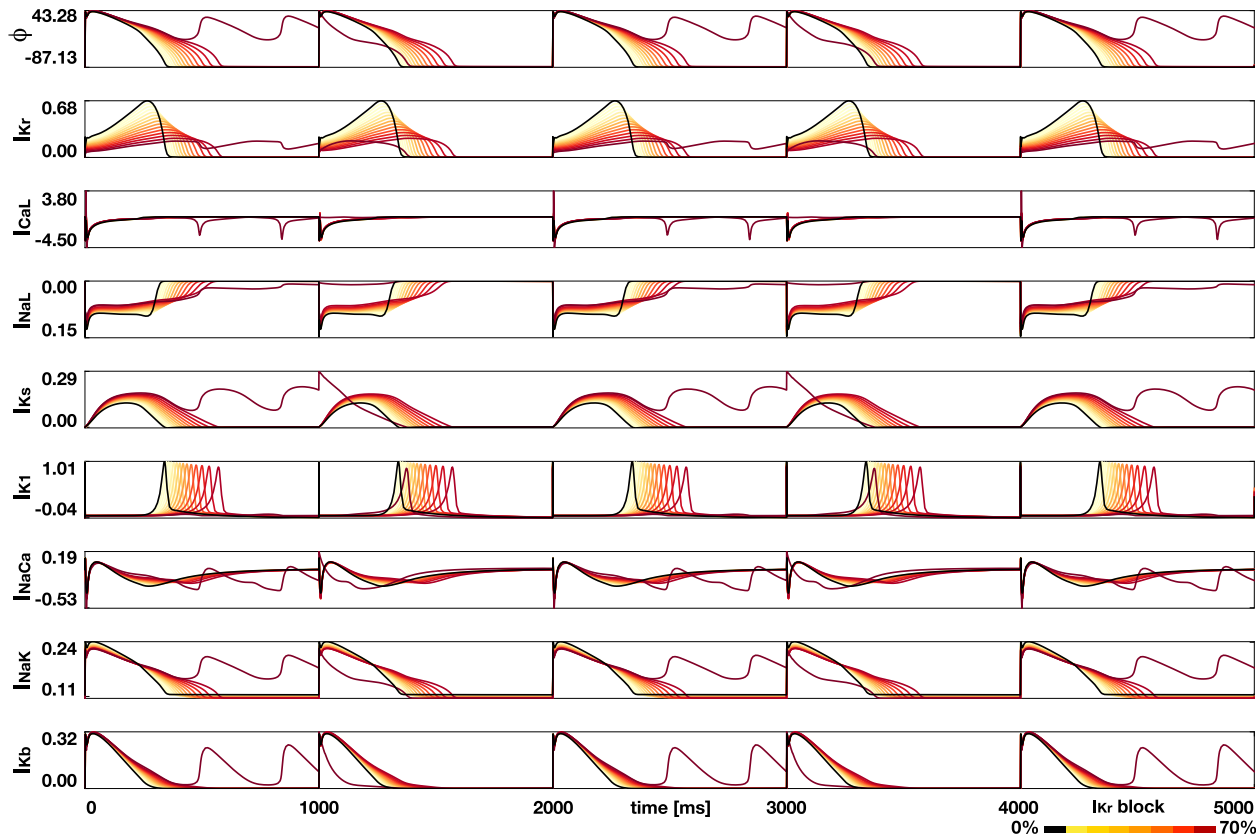


Fig. 4. Effect of dofetilide on the single cell level. Dofetilide modulates the single cell action potential ϕ and the ionic currents I_K , I_{Ca} , and I_{Na} . Black lines represent the baseline potential and currents in midwall cells without the drug, yellow to red lines represent the modified potential and currents for a potassium channel block from $\beta = 10\%$ to 70% in increments of 10% . Blocking the potassium current I_{Kr} prolongs the plateau of the action potential and increases the overall action potential duration. This effect increases with increasing block, from yellow to red. Beyond a critical block of 70% , at a dofetilide concentration of $C = 5.83 \text{ nM}$, midwall cells experience early afterdepolarizations and become self-oscillatory in every other beat, red curves.

five times within the simulated time window of 5000 ms, columns 1 and 7 to 10. Notably, of all profiles, the profiles of the rapid delayed rectifier potassium current I_{Kr} and of the L-type calcium current I_{CaL} most closely resemble the overall action potential profile ϕ , I_{Kr} with a similar sign and I_{CaL} with a reversed sign. Peaks in the action potential ϕ manifest themselves as maxima in the potassium current I_{Kr} and as minima in the calcium current I_{CaL} .

3.5. 65% and 70% I_{Kr} block causes QT interval prolongation, but does not induce torsades de pointes

Figs. 9 and 10 show the evolution of the transmembrane potential ϕ , representative potassium currents I_{Kr} , I_{Ks} , and I_{K1} , and the calcium current I_{CaL} for simulations with a 65% and 70% potassium channel block corresponding to dofetilide concentrations of 2x and 3x. Both electrocardiograms display a regular periodic activation pattern at heart rates of 47 and 46 beats per minute, corresponding to an increase in the R-R interval or cycle length of 28.5% and 30.5% compared to the baseline case in Fig. 8. The QT intervals of both cases are 439 ms and 464 ms, which corresponds to a QT interval prolongation of 62.0% and 71.2% compared to baseline. Similar to the baseline case, during depolarization, the Purkinje network drives the excitation from apex to base with a sharp depolarization front that propagates smoothly across the heart, columns 1 to 2. During repolarization, both ventricles gradually return to their resting state, columns 3 to 6. The excitation pattern repeats itself identically every 1285 ms and 1305 ms, four times within the simulated time window of 5000 ms, columns 1 and 7 to 9.

Strikingly, although we observed early afterdepolarizations for a 70% block at the single cell level in Figs. 4 and 5, we did not see any irregularities or indications of fibrillation for a 70% block at the whole heart level in Fig. 10.

3.6. 75% I_{Kr} block induces torsades de pointes

Figs. 11 and 12 show the evolution of the transmembrane potential ϕ , representative potassium currents I_{Kr} , I_{Ks} , and I_{K1} , and the calcium current I_{CaL} for the simulation with a 75% potassium channel block at a dofetilide concentrations of 4x. Similar to Figs. 8–10, the simulation in Fig. 11 is based on 30% midwall cells, whereas the simulation in Fig. 12 is based on 80% midwall cells. Both electrocardiograms display highly irregular activation patterns at average heart rates of 113 and 115 beats per minute, corresponding to a decrease in the R-R interval or cycle length of 47.0% and 47.5% compared to the baseline case in Fig. 8. The initial QT interval of the 30% midwall cells case in Fig. 11 is 494 ms, which corresponds to a QT interval prolongation of 82.3% compared to baseline. The heart spontaneously transitions into an irregular activation pattern with varying activation fronts characteristic of torsades de pointes. In the one-dimensional model system, midwall cell fractions of 30% and 80% would correspond to the black and red curves in the 75% I_{Kr} block graph in Fig. 6. Surprisingly, although we did not observe early afterdepolarizations for a midwall cell fraction of 30% in the one-dimensional model system in Fig. 6, we did observe a marked rhythm disorder for a 75% block at the whole heart level in Fig. 11.

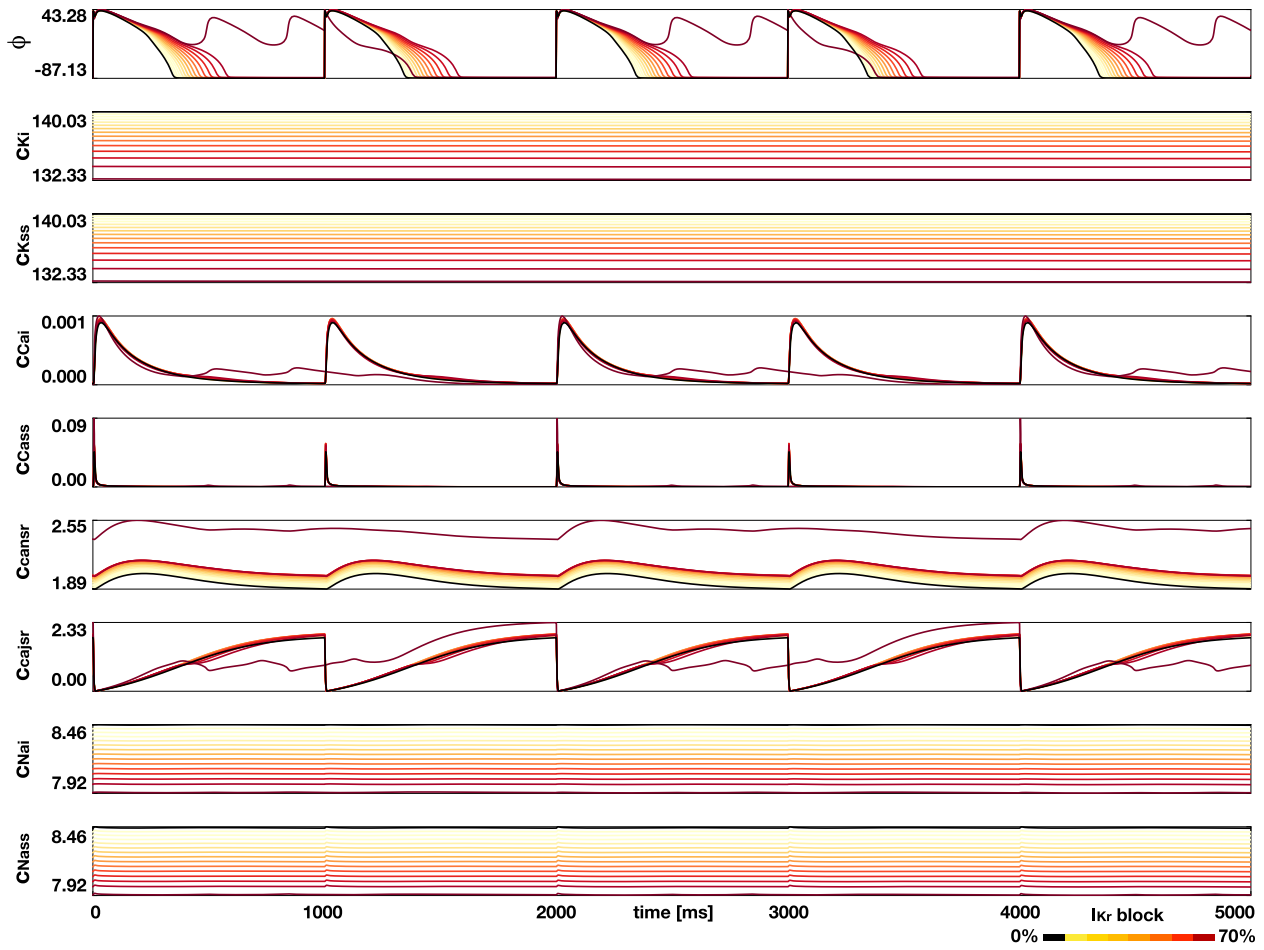


Fig. 5. Effect of dofetilide on the single cell level. Dofetilide modulates the single cell action potential ϕ and the ion concentrations c_K , c_{Ca} , and c_{Na} . Black lines represent the baseline potential and concentrations in midwall cells without the drug, yellow to red lines represent the modified potential and concentrations for a potassium channel block from $\beta = 10\%$ to 70% in increments of 10% . Blocking the potassium current I_{Kr} decreases the potassium and sodium concentrations c_K and c_{Na} . This effect increases with increasing block, from yellow to red. Beyond a critical block of 70% , at a dofetilide concentration of $C = 5.83 \text{ nM}$, midwall cells experience early afterdepolarizations and become self-oscillatory in every other beat, red curves.

Table 1 summarizes the results of our whole heart simulations from Figs. 8–11 and shows the degree of potassium channel block, the corresponding dofetilide concentration, the QT and RR interval lengths, and the heart rate, all in absolute values and as percent changes compared to the baseline simulation with no drugs.

4. Discussion

4.1. Drug safety evaluation can benefit from mechanistic modeling

A serious side effect of many drugs are cardiac arrhythmias in the form of torsades de pointes (Stockbridge et al., 2013). Studies have shown that drugs that block the rapid delayed rectifier potassium current prolong the QT interval in the electrocardiogram, a condition that has historically been associated with a high torsadogenic risk (Redfern et al., 2003). Existing regulatory guidelines therefore focus on monitoring both potassium channel block and QT interval prolongation (Vicente et al., 2016). It is increasingly recognized, however, that these two criteria have a low specificity for the assessment of torsades de pointes (Lancaster and Sobie, 2016; Perrin et al., 2008) and that current regulations that rely on these two biomarkers alone are too conservative (Colatsky et al., 2016). In fact, many safe and potentially useful drugs never make it to the market, and if they do, their labels might be misleading and could discourage physicians to actually prescribe them (Vicente

et al., 2018).

Here we propose to assess torsadogenic risk using an integrative approach that combines drug concentrations, potassium channel block, action potential duration, and QT interval length via mechanistic multiscale modeling. We introduce a computational model that uses drug-induced current block signatures from single cell electrophysiology as input and generates action potential profiles, cardiac excitation patterns, and electrocardiograms as output. We have validated our computational model against cardiac tissue electrophysiology simulators using an N -version benchmark (Niederer et al., 1954) and obtained qualitative and quantitative agreement in both activation times and activation profiles. Of all benchmark codes, our simulations with a benchmark activation time of 38 ms compared most closely to the Chaste code with an activation time of 42 ms (Pathmanathan et al., 2010). By design, our model allows us to explore the interaction of different current blocks (Sahli Costabal et al., 2018a), different drugs (Johannesen et al., 2016), and different cell types across the heart (Sahli Costabal et al., 2018a). Here we focus on the interaction of different cell types in response to a single drug, dofetilide, that selectively blocks a single current, the rapid delayed rectifier potassium current, at varying degrees of block. Specifically, we explore how different cell types—endocardial, mid wall, epicardial, and Purkinje cells—interact to collectively generate a regular healthy excitation pattern across the heart.

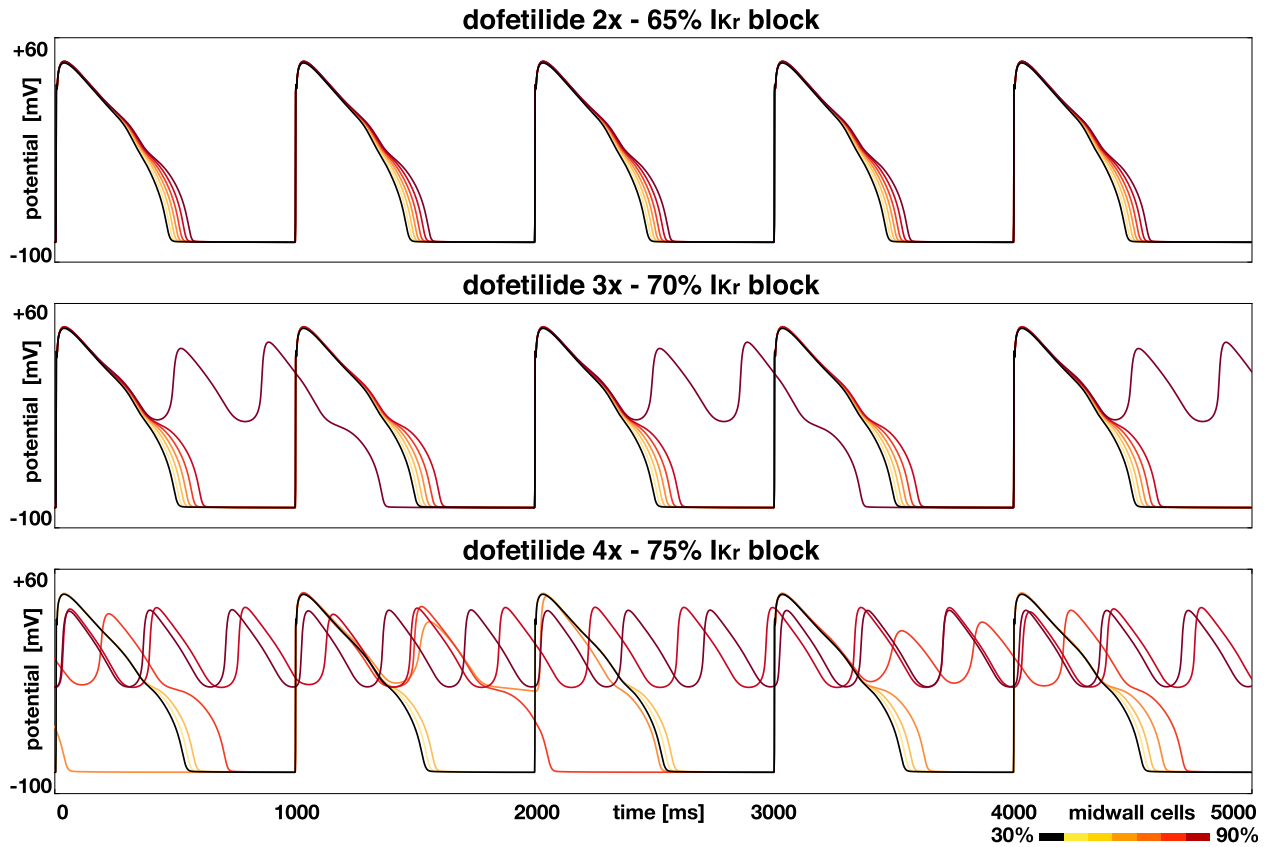


Fig. 6. Effect of dofetilide on the cardiac tissue level. Dofetilide modulates the single cell action potential ϕ recorded at a midwall cell in the center of the one-dimensional cable model. Black lines represent a model with 30% midwall cells representative of the midwall cell fraction in our ventricular model, yellow to red lines represent an increase in midwall cells from 40% to 90% in increments of 10%. The likelihood of early afterdepolarizations increases with increasing dofetilide concentration, from top to bottom, but decreases in the presence of endocardial and epicardial cells, from red to yellow. While midwall cells in isolation display early afterdepolarizations beyond a critical block of 70%, embedded in a cable model, the critical block increases with increasing fractions of stabilizing endocardial and epicardial cells.

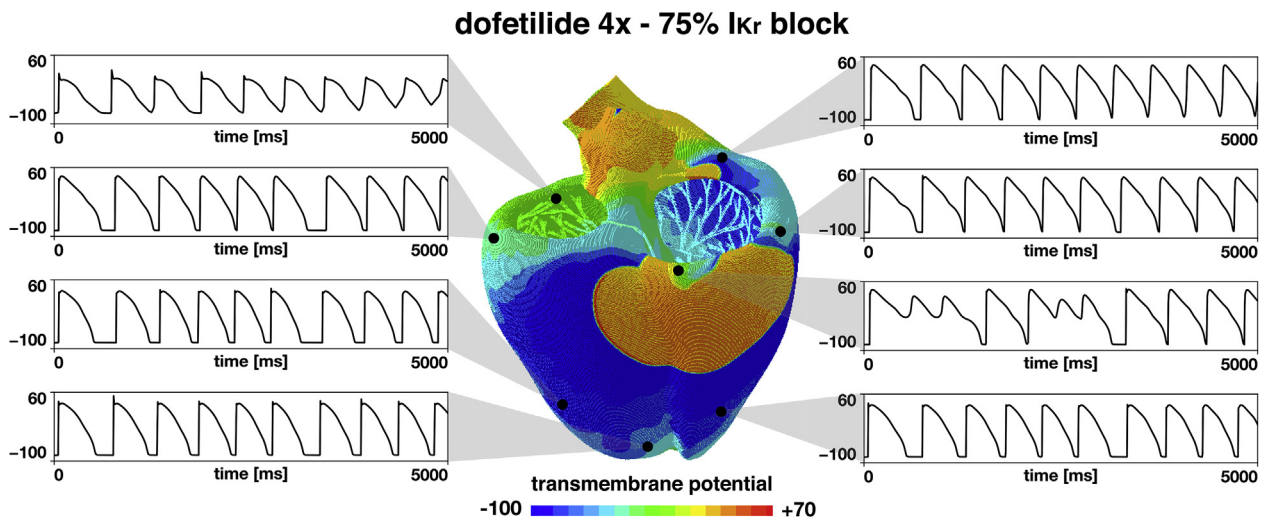


Fig. 7. Effect of dofetilide on the whole heart level. Characteristic snap shot of the transmembrane potential ϕ , and eight local action potentials at 75% potassium channel block corresponding to a dofetilide concentration of 4x. Most cells display a small diastolic interval; some cells display early afterdepolarizations.

4.2. Isolated cells show early afterdepolarizations at 70% I_{Kr} block

Our simulated single cell action potentials, ionic currents, and ion concentrations in Figs. 4 and 5 agree well with the common understanding that, by design, blocking the rapid delayed rectifier

potassium current I_{Kr} prolongs the plateau of the action potential and increases action potential duration (Pfizer, 2011). With increasing drug concentration, the potassium block increases and these effects become more pronounced (Lenz and Hilleman, 2000). In agreement with the literature, beyond a critical drug

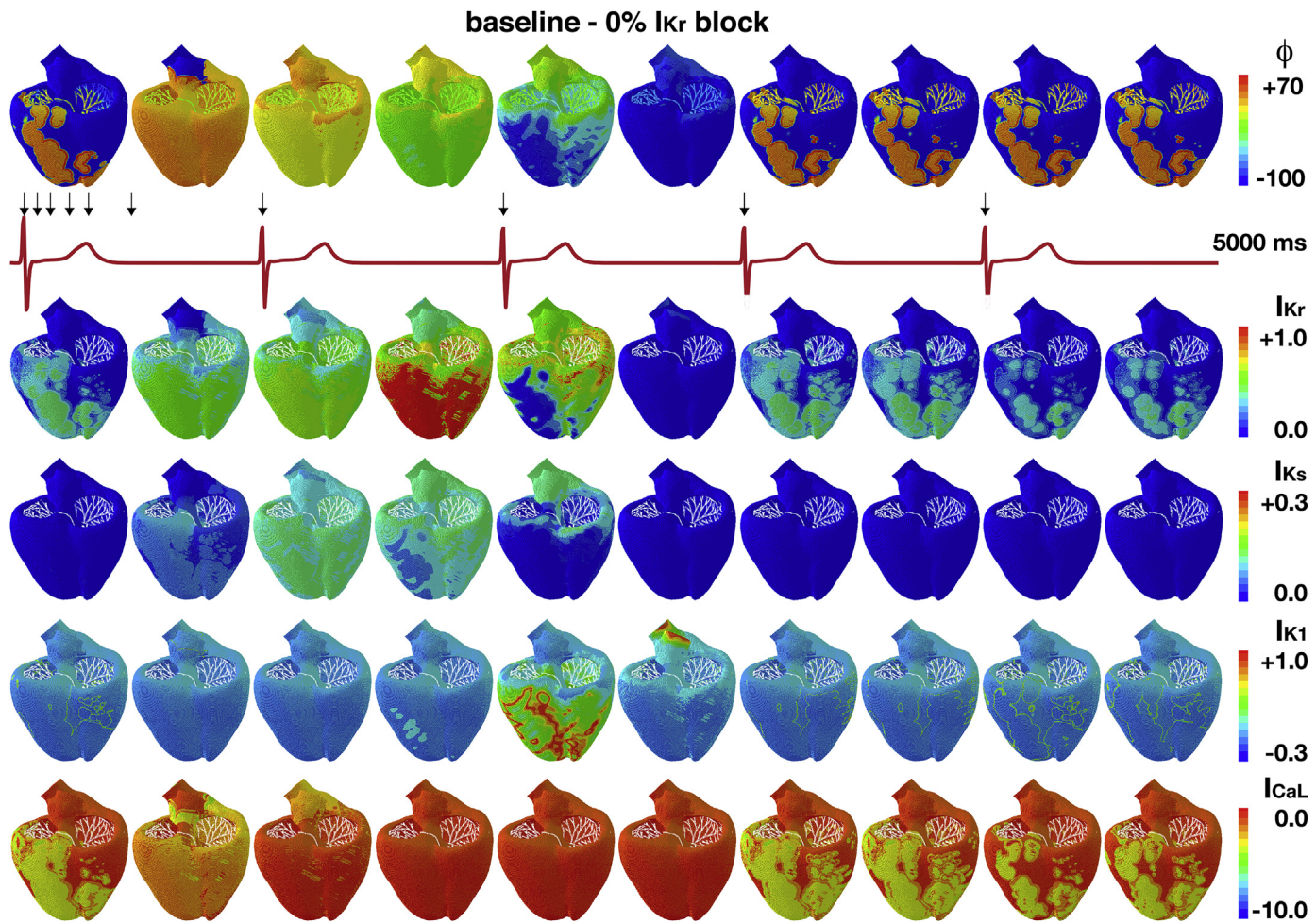


Fig. 8. Effect of dofetilide on the whole heart level. Evolution of the transmembrane potential ϕ , representative potassium currents I_{Kr} , I_{Ks} , and I_{K1} , and the calcium current I_{CaL} at baseline. The red graph shows the electrocardiogram; the black arrows indicate the ten time points associated with the activation profiles. The electrocardiogram displays a regular periodic activation pattern at a heart rate of 60 beats per minute with a QT interval of 271 ms. During depolarization, the Purkinje network drives the excitation from apex to base with a sharp depolarization front that propagates smoothly across the heart, columns 1 to 2. During repolarization, both ventricles gradually return to their resting state, columns 3 to 6. The excitation pattern repeats itself identically every 1000 ms, five times within the simulated time window of 5000 ms, columns 1 and 7 to 10.

concentration, the single cell action potential begins to display early afterdepolarizations. Figs. 4 and 5 nicely capture the characteristic oscillatory potential (Antzelevitch and Sicouri, 1994), and show that these oscillations indirectly affect all voltage-gated channels. While these effects may also be present in endo- and epicardial cells at higher drug concentrations, they typically appear first in midwall cells (Sicouri and Antzelevitch, 1991), which are more vulnerable to drug-induced alternations. To acknowledge the importance of early afterdepolarizations, recent studies suggest to stratify torsadogenic risk based on a two-step classifier that combines experimentally measured I_{Kr} channel block with computationally predicted early afterdepolarizations (Parikh et al., 2017). For our current parameterization (O'Hara et al., 2011a), early afterdepolarizations occur first in midwall cells, beyond a critical I_{Kr} block of 70%, which corresponds to a dofetilide concentration of $C = 5.83 \text{ nM}$ equivalent to 3x the free plasma concentration.

4.3. Early afterdepolarizations are sensitive to tissue heterogeneity

Our one-dimensional model system with endocardial, midwall, and epicardial cells in Fig. 6 confirms that the likelihood of early afterdepolarizations decreases in the presence of endo- and epicardial cells (Xie et al., 2010). Our results agree with the general

notion that, in isolated midwall cells, endogenous membrane currents alone determine the propensity of early afterdepolarizations, whereas in the ventricular wall, early afterdepolarizations are a result of tissue heterogeneity (Akar et al., 2002) and sensitive to both endogenous and exogenous currents (Weiss et al., 2010). Our study reveals that, at 70% I_{Kr} block, at least 90% of midwall cells are required to trigger early afterdepolarizations, while at 75% block, the required midwall cell fraction decreases to 60%. The dynamic interplay between oscillatory midwall cells and non-afterdepolarizing endo- and epicardial cells is often referred to as source-sink mismatch (Sato et al., 2009). From a pathophysiological point of view, this source-sink interaction is powerful mechanism to protect the healthy heart from sporadic episodes of torsades de pointes (Weiss et al., 2010). The obvious question to ask is how many contiguous early afterdepolarizing cells are required to generate a polymorphic ventricular tachycardia that propagates into the surrounding non-afterdepolarizing tissue? In our model system, we represent a transmural section of the ventricular wall by 100 healthy adult ventricular cardiomyocytes of 100 μm length. Our simulations require 90 early afterdepolarizing midwall cells at 70% I_{Kr} block and 60 early afterdepolarizing midwall cells at 75% I_{Kr} block. For comparison, a recent one-dimensional study found that at least 70 early afterdepolarizing cells were necessary to propagate

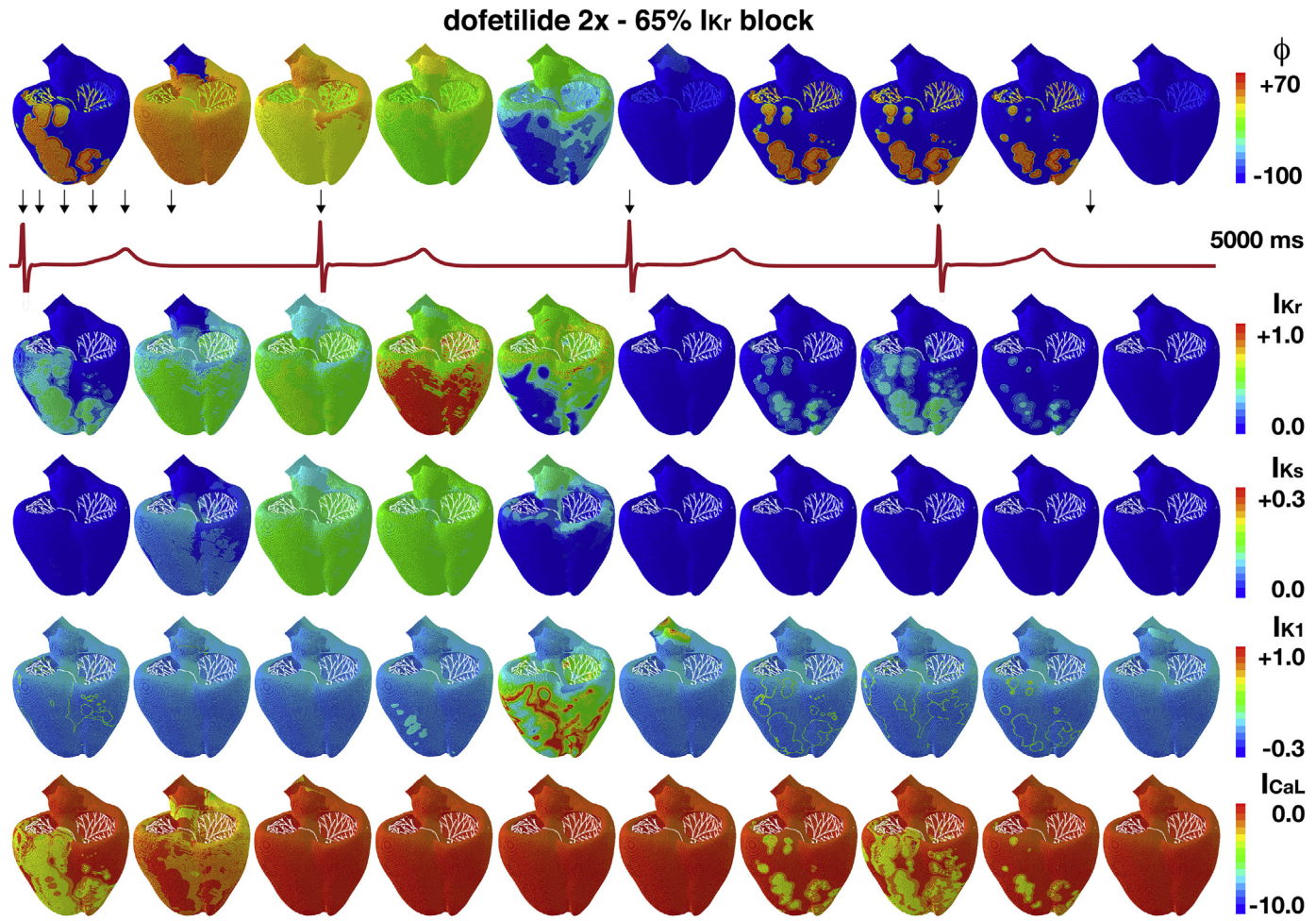


Fig. 9. Effect of dofetilide on the whole heart level. Evolution of the transmembrane potential ϕ , representative potassium currents I_{Kr} , I_{ks} , and I_{K1} , and the calcium current I_{CaL} at 65% potassium channel block corresponding to a dofetilide concentration of 2x. The red graph shows the electrocardiogram; the black arrows indicate the ten time points associated with the activation profiles. The electrocardiogram displays a regular periodic activation pattern at a heart rate of 47 beats per minute with a QT interval of 439 ms. During depolarization, the Purkinje network drives the excitation from apex to base with a sharp depolarization front that propagates smoothly across the heart, columns 1 to 2. During repolarization, both ventricles gradually return to their resting state, columns 3 to 6. The excitation pattern repeats itself identically every 1,285 ms, four times within the simulated time window of 5000 ms, columns 1 and 7 to 9.

the new wavefront into the surrounding tissue (Xie et al., 2010). While these numbers are in excellent qualitative and quantitative agreement, an important open question is how do these one-dimensional estimates translate into the three-dimensional heart?

4.4. Prolonged QT intervals do not necessarily trigger torsades

To address this question, in Fig. 8, we first created a baseline excitation profile of the left and right ventricles that agrees well with the excitation sequence in the healthy human heart. Fig. 8 also illustrates the interaction of the transmembrane potential and the most relevant ionic currents. By design of our cell model (O'Hara et al., 2011a), peaks in the excitation profile correspond to maxima in the potassium current I_{Kr} and to minima in the calcium current I_{CaL} . A critical contributor to healthy excitation is the Purkinje fiber network that quickly and reliably transmits the signal from the atrioventricular node down the endocardium to collectively excite the heart from apex to base (Sahli Costabal et al., 2016a). After 72 ms, the ventricles are fully activated, which agrees well with the depolarization times in healthy human hearts that vary between 62 ms and 80 ms (Durrer et al., 1970). The QT interval measures 271 ms and after less than 400 ms, the ventricles

are completely depolarized. According to Fig. 1, our Purkinje cells display an inherent automaticity at a frequency of 60 beats per minute (Stewart et al., 2009a). In the absence of drugs, this results in identical excitation patterns, which repeat themselves every 1000 ms, five times within the simulated time window of 5000 ms. This raises the question how precisely do different concentrations of drugs modulate these excitation times?

To characterize the effects of dofetilide on the cardiac excitation patterns, we block the rapid delayed rectifier potassium current by 65%, 70%, and 75% according to the block-concentration diagram in Fig. 3. The corresponding simulations at dofetilide concentrations of 2x, 3x, and 4x in Figs. 9–11 agree well with the label of Tikosyn (Pfizer, 2011) and with the results of clinical studies in patients (Abraham et al., 2015). They support the common notion that, at low doses, dofetilide is a safe and effective drug with low pro-arrhythmic risk (Pfizer, 2011). At 2x and 3x, in Figs. 9 and 10, the heart rate decreases from 60 beats per minute at baseline to 47 and 46 beats per minute, a reduction of -21.7% and -23.3%. These are well known side effects of dofetilide (Lenz and Hilleman, 2000). In agreement with a recent clinical study that reported a QT prolongation of 79 ms (Johannesen et al., 2014), our simulation predicts a substantial but safe prolongation of the effective refractory period.

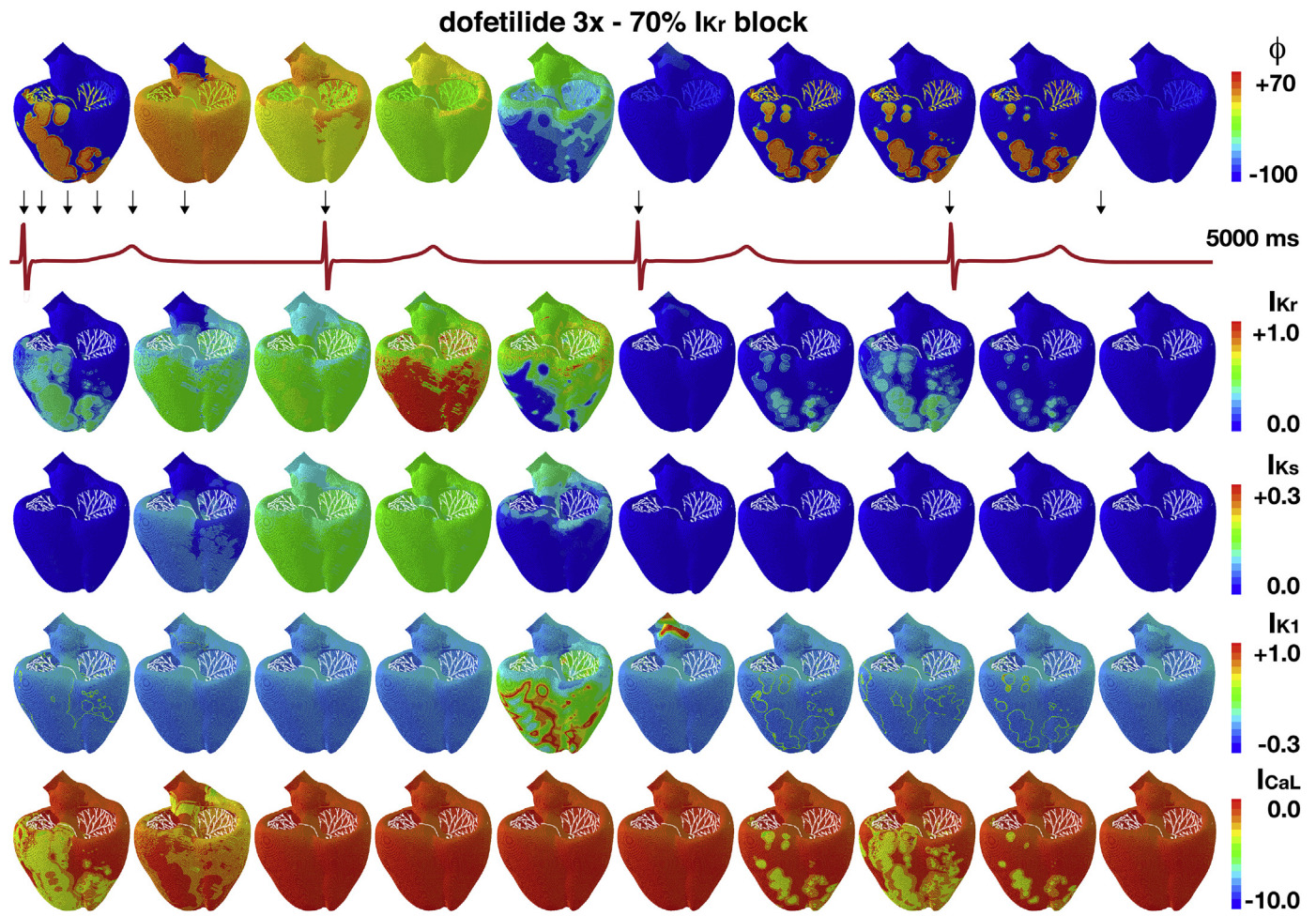


Fig. 10. Effect of dofetilide on the whole heart level. Evolution of the transmembrane potential ϕ , representative potassium currents I_{K_r} , I_{K_s} , and I_{K_1} , and the calcium current I_{CaL} at 70% potassium channel block corresponding to a dofetilide concentration of 3x. The red graph shows the electrocardiogram; the black arrows indicate the ten time points associated with the activation profiles. The electrocardiogram displays a regular periodic activation pattern at a heart rate of 46 beats per minute with a QT interval of 464 ms. During depolarization, the Purkinje network drives the excitation from apex to base with a sharp depolarization front that propagates smoothly across the heart, columns 1 to 2. During repolarization, both ventricles gradually return to their resting state, columns 3 to 6. The excitation pattern repeats itself identically every 1305 ms, four times within the simulated time window of 5000 ms, columns 1 and 7 to 9.

Dofetilide concentrations of 2x and 3x prolong the QT interval to 439 ms and 464 ms, an increase of 62.0% and 71.2% compared to the baseline case in Fig. 8. However, at both concentrations, the heart maintains its regular sinus rhythm. This finding is in contrast with the critical dofetilide concentration of 3x at which midwall cells display early afterdepolarizations in Figs. 4 and 5, but in line with the source-sink hypothesis (Sato et al., 2009) according to which a sufficient number of afterdepolarizing cells is required to trigger arrhythmogenesis in Fig. 6.

4.5. Whole heart models show torsadogenesis at 75% I_{K_r} block

At a dofetilide concentration of 4x in Fig. 11, the heart rate increases drastically from 60 to 113 beats per minute, an increase of +88.3%. The spontaneous transition from a regular beat into a sequence of rapid, irregular QRS complexes is a classical hallmark of torsades de pointes (Dessertenne, 1966). The initial QT interval measures 494 ms, a significant increase of 82.3% compared to baseline, but a relatively moderate increase compared to the 464 ms for the 3x case. At a dofetilide concentration of 4x, only midwall cells experience early afterdepolarizations (Sahli Costabal et al., 2018b), while endocardial, epicardial and Purkinje cells display a regular, yet prolonged, action potential profile. While 30%

of afterdepolarizing midwall cells are sufficient to spontaneously initiate an episode of torsades de pointes in the whole heart in Fig. 11, the corresponding one-dimensional model in Fig. 6 maintains its regular rhythm even up to 50% of midwall cells. This discrepancy agrees well with recent studies that report a requirement of 70 early afterdepolarizing cells in one-dimensional simulations, 6940 in two-dimensional simulations, and 696,910 in three-dimensional simulations to propagate early afterdepolarizations into the surrounding tissue (Xie et al., 2010). In the thin layer of midwall cells in the ventricular wall, endocardial and epicardial cells can overwrite the early afterdepolarizations and the transmembrane potential varies within its full range between -100 mV and $+70$ mV. In the region near the great vessels, electric coupling between a sufficiently large neighborhood of midwall cells synchronizes chaotic early afterdepolarizations over a characteristic spatial scale (Sato et al., 2009) in which the transmembrane potential freezes near 0 mV. The interaction of these regions of chaos and coupling generates islands of early afterdepolarizations embedded in regularly excited tissue, which shift on a beat-to-beat basis (Weiss et al., 2010). In Fig. 11 this shift is most dramatic between the sixth and seventh beat and is clearly visible, both in the excitation pattern and in the electrocardiogram. These shifting early afterdepolarizing regions overwrite the

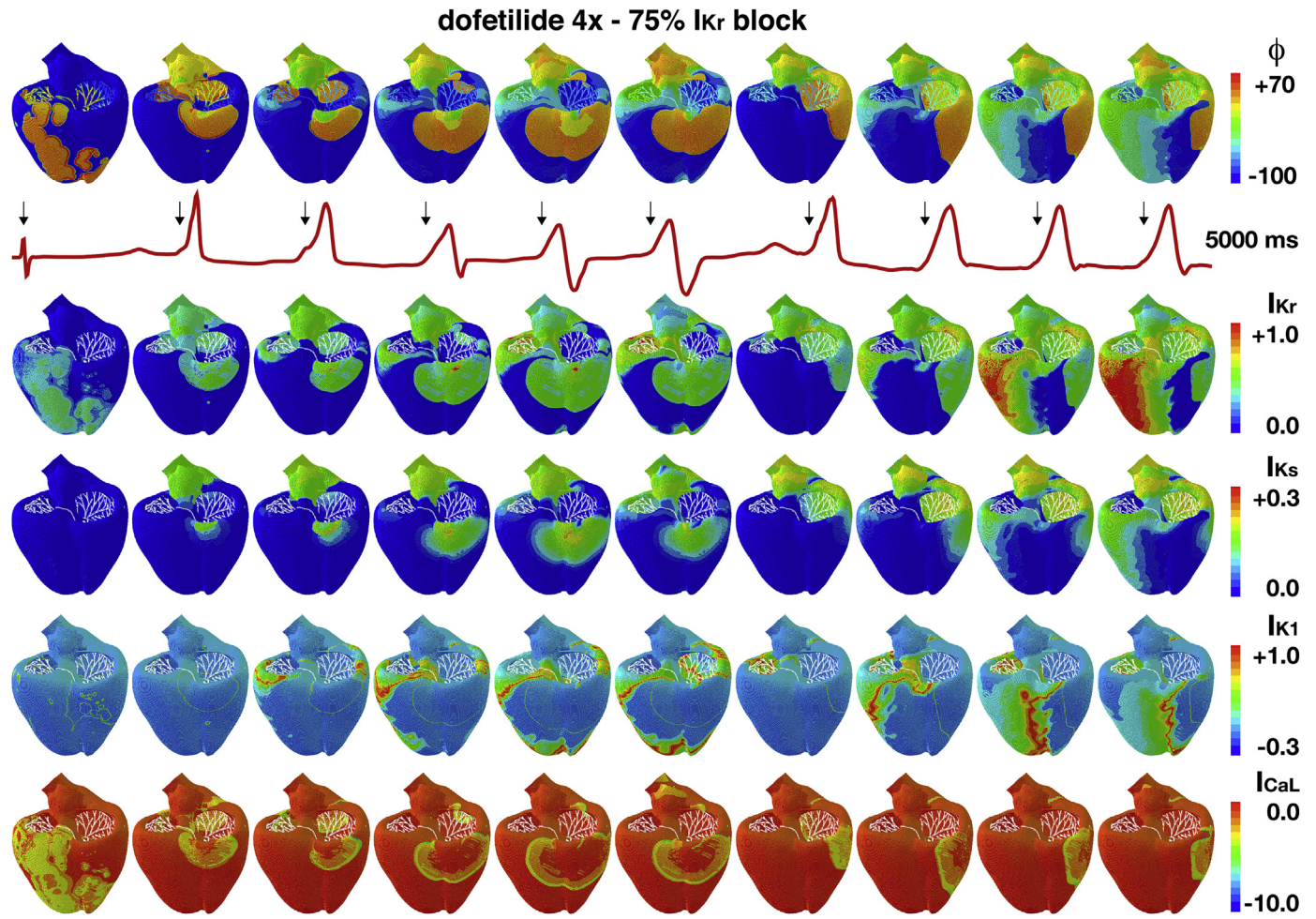


Fig. 11. Effect of dofetilide on the whole heart level. Evolution of the transmembrane potential ϕ , representative potassium currents I_{K_R} , I_{K_S} , and I_{K_1} , and the calcium current I_{CaL} at 75% potassium channel block corresponding to a dofetilide concentration of 4x. The red graph shows the electrocardiogram; the black arrows indicate the ten time points associated with the activation profiles. During the first depolarization, the Purkinje network drives the excitation from apex to base with a sharp depolarization front that propagates smoothly across the heart, column 1. After a markedly prolonged QT interval of 494 ms, the propagation of the excitation wave spontaneously becomes irregular and asynchronous. The next five activation fronts are initiated in the right posterior basal region, columns 2 to 6, and the following four fronts are initiated in the right lateral wall, columns 7 to 10. This transition from one excitation pattern into another is clearly visible between the sixth and seventh peak in the electrocardiogram. The overall excitation is no longer driven by the Purkinje network, but by excitation fronts that activate the heart in irregular patterns associated with a sequence of rapid, widened irregular QRS complexes, all characteristic features of torsades de pointes. The average heart rate has nearly doubled to 113 beats per minute.

activation of the Purkinje fiber network and excite the heart in chaotic twisting patterns, a classical hallmark of torsades de pointes (Dessertenne, 1966).

4.6. Torsadogenesis is sensitive to tissue heterogeneity

In Figs. 9–11, we have assumed a generic distribution of 20% endocardial cells, 30% midwall cells, and 50% epicardial cells (Sahli Costabal et al., 2018a). Tissue heterogeneity is particularly important in view of the local distribution of midwall cells (Sicouri and Antzelevitch, 1991), which display the highest dose-response sensitivity of all ventricular cells, and are most closely associated with early afterdepolarizations and torsadogenesis (Antzelevitch and Sicouri, 1994). To demonstrate the sensitivity of our torsadogenic risk assessment with respect to the midwall cell distribution (Akar et al., 2002), we performed a similar simulation as in Fig. 11, at a dofetilide concentration of 4x and an I_{K_R} block of 75%, but now with 10% endocardial cells, 80% midwall cells, and 10% epicardial cells. The resulting transmembrane potential and electrocardiogram in Fig. 12 differ markedly from Fig. 11: They including several dynamically shifting local foci (Weiss et al., 2010) that initiate

multiple interacting excitation fronts. This agrees well with the reported chaotic excitation during an episode of torsades de pointes, where focal activations emerge from multiple discrete sites, which shift spontaneously and vary dynamically in time and space (Sato et al., 2009). Strikingly, despite a similar fraction of 80% midwall cells, the response of the three-dimensional heart in Fig. 12 differs significantly from the response of the one-dimensional model in Fig. 6: In the one-dimensional model, the transmembrane potential oscillates tightly around the zero state at a regular frequency of 168 beats per minute. In the three-dimensional heart, these tight oscillations are locally constrained to a region near the great vessels with a high density of midwall cells, while the ventricular walls alternate between depolarized and repolarized states; yet, at a much lower rate of 115 beats per minute. While one-dimensional models that mimic transmural cell heterogeneity have recently emerged as an efficient surrogate models for whole heart simulations (Beattie et al., 2013; Sadrieh et al., 2014; Di Veroli et al., 2014) our study suggests that the results of these cable models do not directly translate into real heart models and should therefore be interpreted with the necessary care and thought.

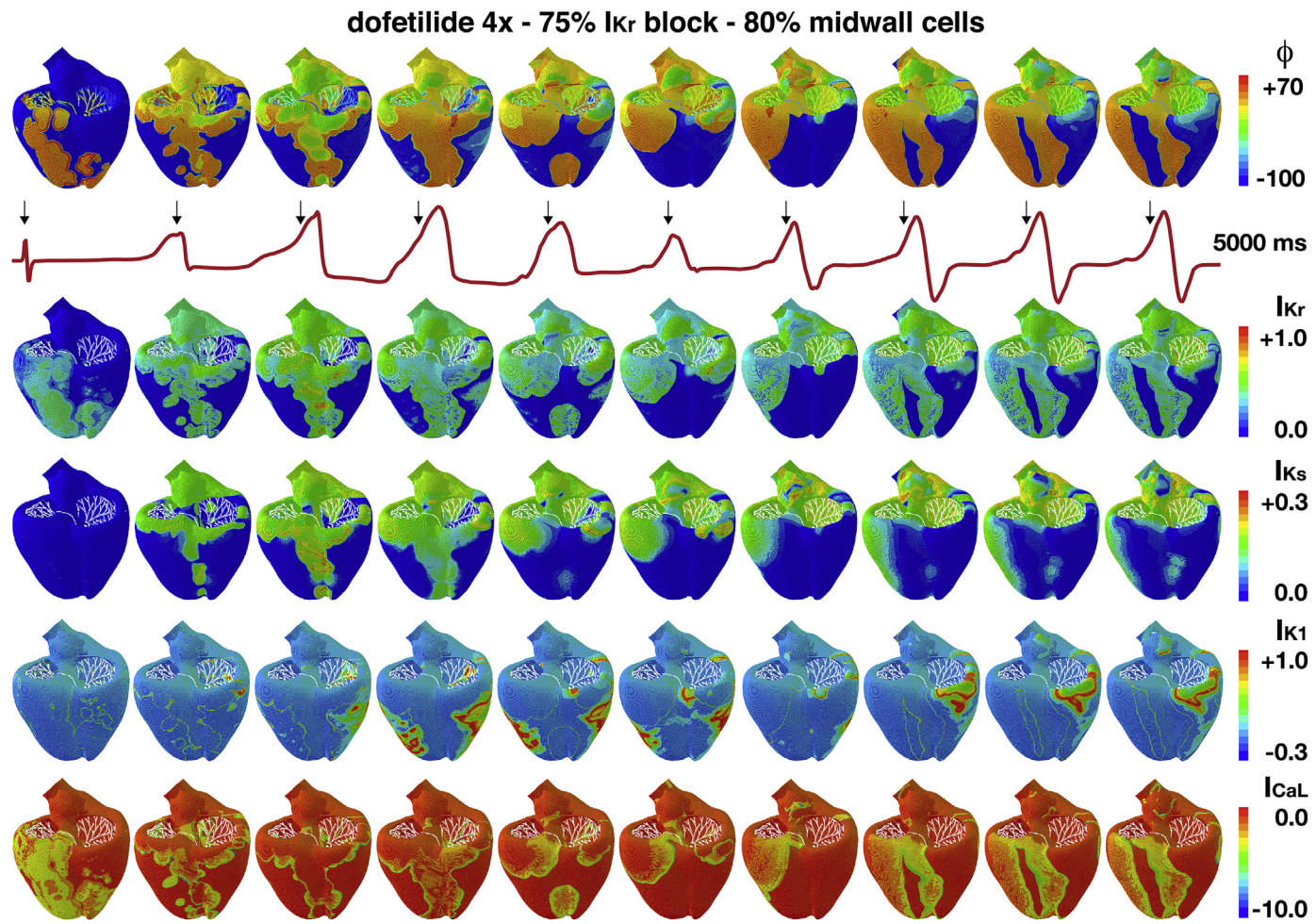


Fig. 12. Effect of dofetilide on the whole heart level. Evolution of the transmembrane potential ϕ , representative potassium currents I_{K_r} , I_{K_s} , and I_{K_1} , and the calcium current I_{CaL} at 75% potassium channel block corresponding to a dofetilide concentration of 4x for a heart model with 80% midwall cells. The red graph shows the electrocardiogram; the black arrows indicate the ten time points associated with the activation profiles. During the first depolarization, the Purkinje network drives the excitation from apex to base with a sharp depolarization front that propagates smoothly across the heart, column 1. The propagation of the excitation wave spontaneously becomes irregular and asynchronous. The next three activation fronts are initiated at the septum, columns 2 to 4, followed by the apex and base, column 5, followed by the left lateral wall, columns 6 to 10. The overall excitation is no longer driven by the Purkinje network, but by excitation fronts that activate the heart in irregular patterns associated with a sequence of rapid, widened irregular QRS complexes, all characteristic features of torsades de pointes. The average heart rate has nearly doubled to 115 beats per minute.

Table 1

Degree of potassium channel block, dofetilide concentration, QT and RR interval lengths and heart rate, and their percent changes with respect to baseline for drug simulations in Figs. 8–11.

I_{K_r}	dofetilide		QT		RR		heart	
block	concentration	[nM]	interval	[ms]	interval	[ms]	[bpm]	rate
[%]	x		[%]		[%]		[%]	
0%	0.00	0.00	271	0.0	1000	0.0	60	0.0
65%	4.08	1.94	439	+62.0	1285	+28.5	47	-21.7
70%	5.83	2.77	464	+71.2	1305	+30.5	46	-23.3
75%	8.63	4.11	494	+82.3	530	-47.0	113	+88.3

4.7. Limitations

Although our study provides new insight into the importance of early afterdepolarizations, the role of midwall cells, and the relevance of tissue heterogeneity in the genesis of torsades de pointes, it has several important limitations that we need to keep in mind when interpreting its results: First and foremost, our study uses the original O'Hara Rudy model (O'Hara et al., 2011a) combined with a simple pore block in equations (8) and (9). An important but

computationally rather straightforward next step would be to use a more advanced dynamic channel block model that would account for trapping compounds with high torsadogenic risk and show a stronger reverse use dependency of action potential prolongation (Li et al., 2017). Second, the major unknowns in arrhythmogenic risk assessment are pharmacodynamic variability caused by variability in drug action at the cellular, tissue, whole-organ, and whole organism levels and pharmacokinetic variability caused by variability in concentration at the target site of action (Roden, 2016).

Both are essentially inputs to our model (Crumb et al., 2016), summarized in Fig. 3, and can be easily generalized to include more variability once this information becomes available. In the extreme case, we could even personalize the block-concentration response and parameterize our model for personalized drug screening. Third, while our electrocardiograms in the presence of large doses of dofetilide do display several characteristic features of torsades de pointes, their heart rates of 113 and 115 beats per minute are rather on the low end for a ventricular tachycardia in the form of torsades de pointes. We will attempt to address this issue in the future and will also perform longer simulations than just 5000 ms to explore whether the heart would naturally return to a regular rhythm. Fourth, while our current study is limited to a single drug that selectively blocks a single channel, our model can be equally used to study the effect of drugs that block several interacting channels, as we have recently shown (Sahli Costabal et al., 2018a), or the effect of co-administration of several compensatory drugs (Johannesen et al., 2016). Fifth, ideally, we would personalize the human heart geometry, and, probably even more importantly, the cellular heterogeneity across the ventricular wall to more accurately assess the local origin of torsades de pointes. However, even without personalized pharmacodynamics, pharmacokinetics, and personalized heart models (Chabiniok et al., 2016), we can already use our current model to perform sensitivity analyses (Sher et al., 2010) and uncertainty quantifications (Chang et al., 2017) and predict an arrhythmogenic risk regime that will provide more holistic insight than a single risk quantifier.

5. Conclusion

Many drugs, not just cardiac drugs, can have serious side effects in the form of torsades de pointes, a special type of ventricular tachycardia that can lead to sudden cardiac death. Current regulatory paradigms focus on monitoring the degree of potassium channel block and the length of the QT interval as characteristic biomarkers to assess torsadogenic risk. However, not all drugs that prolong the QT interval will actually induce torsade de pointes and the QT interval alone seems to be a poor indicator for drug screening. Here we establish a multiscale exposure-response simulator that uses block-concentration characteristics as input and creates excitation profiles and electrocardiograms as output. We illustrate the potential of our simulation tool for the example of a common but controversial drug, dofetilide. At dofetilide concentrations of 2x and 3x, our model predicts a significant increase the QT interval by 62.0% and 71.2%, yet, without any sign of torsades de pointes. At a dofetilide concentration of 4x, the QT interval increases by 82.3% and the model spontaneously develops torsades de pointes. Interestingly, this critical drug concentration of 4x is higher than the critical concentration estimated from early after-depolarizations in single cells and lower than in one-dimensional cable models. Our results emphasize the importance of whole heart modeling and can help explain why current regulatory paradigms fail to accurately assess the pro-arrhythmic risk of a drug. Beyond the more holistic risk assessment of existing drugs, our multiscale exposure-response simulations can provide insight into the co-administration of existing drugs and, ultimately, guide the design of safer drugs towards reducing life threatening drug-induced rhythm disorders in the heart.

Disclosures

Jiang Yao is an employee of Dassault Systèmes Simulia Corporation, the company that has founded the Living Heart Project of which the geometry was used in the present study. Anna Sher is an employee of Pfizer Inc., the pharmaceutical company that is

marketing the drug dofetilide used in the present study under the trade name Tikosyn.

Funding

This study was supported by a Stanford Cardiovascular Institute seed grant and by the Becas Chile-Fulbright Fellowship to Francisco Sahli Costabal and by the Stanford Bio-X IIP seed grant "A Novel Approach Towards Drug Screening" and the National Institutes of Health Grant U01 HL119578 to Ellen Kuhl. This work used the Extreme Science and Engineering Discovery Environment XSEDE supported by National Science Foundation grant number ACI-1548562.

Acknowledgments

The computational model was developed within the Living Heart project. We acknowledge the Zygote Media Group for providing the anatomic model and Dassault Systèmes SIMULIA, Uber Cloud, Advania, and Hewlett Packard Enterprise for providing the computational resources for our simulations.

Appendix A. Supplementary data

Supplementary data to this article can be found online at <https://doi.org/10.1016/j.pbiomolbio.2018.10.003>.

Transparency document

Transparency document related to this article can be found online at <https://doi.org/10.1016/j.pbiomolbio.2018.10.003>.

References

- Abbasi, M., Small, B.G., Patel, N., Jamei, M., Polak, S., 2017. Early assessment of proarrhythmic risk of drugs using the *in vitro* data and single-cell-based *in silico* models: proof of concept. *Toxicol. Mech. Methods* 27, 88–99.
- Abraham, J.E.M., Saliba, W.I., Vekstein, C., Lawrence, D., Bhargava, M., Bassiouny, M., Janiszewski, D., Lindsay, B., Militello, M., Nissen, S.E., Poe, S., Tanaka-Esposito, C., W.K., Wilkoff, B.L., 2015. Safety of oral dofetilide for rhythm control of atrial fibrillation and atrial flutter. *Circulation: Arrhythm. Electrophysiol.* 8, 772–776.
- Akar, F.G., Yan, G.X., Antzelevitch, C., Rosenbaum, D.S., 2002. Unique topographical distribution of M cells underlies reentrant mechanism of torsade de pointes in the long-QT syndrome. *Circulation* 105, 1247–1253.
- Allen LaPointe, N.M., Chen, A., Hammill, B., DeLong, E., Kramer, J.M., Califf, R.M., 2003. Evaluation of the dofetilide risk-management program. *Am. Heart J.* 146, 894–901.
- Antzelevitch, C., Sicouri, S., 1994. Clinical relevance of cardiac arrhythmias generated by afterdepolarizations: role of M cells in the generation of U waves, triggered activity and torsade de pointes. *J. Am. Coll. Cardiol.* 23, 259–277.
- Baillargeon, B., Rebelo, N., Fox, D., Taylor, R., Kuhl, E., 2014. The Living Heart Project: a robust and integrative simulator for human heart function. *Eur. J. Mech. Solid.* 48, 38–47.
- Beattie, K., Luscombe, C., Williams, G., Munoz-Muriedas, J., Gavaghan, D., Cui, Y., Mirams, G., 2013. Using ion channel screening data to predict QT interval changes in the rabbit ventricular wedge. *J. Pharmacol. Toxicol. Methods* 68 (1), 88–96.
- Bohnen, M.S., Peng, G., Robey, S.H., Terrenoire, C., Iyer, V., Sampson, K.J., Kass, R.S., 2017. Molecular pathophysiology of congenital long QT syndrome. *Physiol. Rev.* 97, 89–134.
- Bordas, R.M., Gillow, K., Gavaghan, D., Rodriguez, B., Kay, D., 2012. A bidomain model of the ventricular specialized conduction system of the heart. *SIAM J. Appl. Math.* 72 (5), 1618–1643.
- Briceno, D.F., Supple, G.E., 2017. Dofetilide reloaded: to admit or not to admit, that is the question. *Circulation: Arrhythm. Electrophysiol.* 10, e005815.
- Chabiniok, R., Wang, V., Hadjicharalambous, M., Asner, L., Lee, J., Sermesant, M., Kuhl, E., Young, A., Moireau, P., Nash, M., Chapelle, D., Nordsletten, D., 2016. Multiphysics and multiscale modeling, data-model fusion and integration of organ physiology in the clinic: ventricular cardiac mechanics. *Interface Focus* 6, 20150083.
- Chang, K.C., Dutta, S., Mirams, G.R., Beattie, K.A., Sheng, J., Tran, P.N., Wu, M., Wu, W.W., Cotlasky, T., Strauss, D.G., Li, Z., 2017. Uncertainty quantification reveals the importance of data variability and experimental design considerations for *in silico* proarrhythmia risk assessment. *Front. Physiol.* 8, 917.

- Colatsky, T., Fermini, B., Gintant, G., Pierson, J., Sager, P., Sekino, Y., Strauss, D., Stockbridge, N., 2016. The comprehensive in vitro proarrhythmia assay (CiPA) initiative – update on progress. *J. Pharmacol. Toxicol. Methods* 81, 15–20.
- Crumb, W., Vicente, J., Johannesen, L., Strauss, D., 2016. An evaluation of 30 clinical drugs against the comprehensive in vitro proarrhythmia assay (CiPA) proposed ion channel panel. *J. Pharmacol. Toxicol. Methods* 81, 251–262.
- Dassault Systèmes, 2017. SIMULIA, Abaqus 2017, Documentation. Dassault Systèmes, Rhode Island.
- Dessertenne, F., 1966. La tachycardie ventriculaire a deux foyers oppose variables. *Arch. Mal. Coeur. Vaiss.* 59, 263–272.
- Di Veroli, G.Y., Davies, M.R., Zhang, H., Abi-Gerges, N., Boyett, M.R., 2014. HERG inhibitors with similar potency but different binding kinetics do not pose the same proarrhythmic risk: implications for drug safety assessment. *J. Cardiovasc. Electrophysiol.* 25, 197–207.
- DiMasi, J.A., Hansen, R.W., Grabowski, H.G., 2003. The price of innovation: new estimates of drug development cost. *J. Health Econ.* 22, 151–185.
- DiMasi, J.A., Grabowski, H.G., Hansen, R.W., 2016. Innovation in the pharmaceutical industry: new estimations of R&D cost. *J. Health Econ.* 47, 20–33.
- Durrer, D., van Dam, R.T., Freud, G.E., Janse, M.J., Meijler, F.L., Arzbaecher, R.C., 1970. Total excitation of the isolated human heart. *Circulation* 41 (6), 899–912.
- Dutta, S., Michole, A., Zucur, E., Quinn, T.A., Taggart, P., Rodriguez, B., 2016. Early afterdepolarizations promote transmural reentry in ischemic human ventricle with reduced repolarization reserve. *Prog. Biophys. Mol. Biol.* 120, 236–248.
- Fink, M., Noble, D., Virág, L., Varró, A., Giles, W.R., 2008. Contributions of HERG K⁺ current to repolarization of the human ventricular action potential. *Prog. Biophys. Mol. Biol.* 96, 357–376.
- Fink, M., Niederer, S.A., Cherry, E.M., Fenton, F.H., Koivumaki, J.T., Seemann, G., Thul, R., Zhang, H., Sachse, F.B., Beard, D., Crampin, E.J., Smith, N.P., 2011. Cardiac cell modelling: observations from the heart of the cardiac physiome project. *Prog. Biophys. Mol. Biol.* 104, 2–21.
- Gintant, G., Sager, P., Stockbridge, N., 2016. Evolution of strategies to improve pre-clinical cardiac safety testing. *Nature Reviews. Drug Discovery* 15 (7), 1–15.
- Göktepe, S., Kuhl, E., 2009. Computational modeling of cardiac electrophysiology: a novel finite element approach. *Int. J. Numer. Methods Eng.* 79, 156–178.
- Göktepe, S., Wong, J., Kuhl, E., 2010. Atrial and ventricular fibrillation: computational simulation of spiral waves in cardiac tissue. *Arch. Appl. Mech.* 80 (5), 569–580.
- Johannesen, L., Vicente, J., Mason, J., Sanabria, C., Waite-Labott, K., Hong, M., Guo, P., Lin, J., Sørensen, J., Galeotti, L., Florian, J., Ugander, M., Stockbridge, N., Strauss, D., 2014. Differentiating drug-induced multichannel block on the electrocardiogram: randomized study of dofetilide, quinidine, ranolazine, and verapamil. *Clin. Pharmacol. Ther.* 96 (5), 549–558.
- Johannesen, L., Vicente, J., Mason, J.W., Sanabria, C., Waite-Labott, K., Hong, M., Lin, J., Guo, P., Mutlib, A., Wang, J., Crumb, W.J., Blinova, K., Chan, D., Stohlman, J., Florian, J., Ugander, M., Stockbridge, N., Strauss, D.G., 2016. Late sodium current block for drug-induced long QT syndrome: results from a prospective clinical trial. *Clin. Pharmacol. Ther.* 99, 214–223.
- Kotikyanadanam, M., Göktepe, S., Kuhl, E., 2010. Computational modeling of electrocardiograms: a finite element approach toward cardiac excitation. *Int. J. Numerical Method. Biomed. Eng.* 26, 524–533.
- Krogh-Madsen, T., Jacobson, A.F., Ortega, F.A., Christini, D.J., 2017. Global optimization of ventricular myocyte model to multi-variable objective improves predictions of drug-induced torsades de pointes. *Front. Physiol.* 8, 1059.
- Lancaster, M.C., Sobie, E.A., 2016. Improved prediction of drug-induced torsades de pointes through simulations of dynamics and machine learning algorithms. *Clin. Pharmacol. Ther.* 100, 371–379.
- Lenz, T.L., Hilleman, D.E., 2000. Dofetilide, a new class III antiarrhythmic agent. *Pharmacotherapy* 20, 776–786.
- Li, Z., Dutta, S., Sheng, J., Tran, P.N., Wu, W., Chang, K., Mdluli, T., Strauss, D.G., Colatsky, T., 2017. Improving the in silico assessment of proarrhythmia risk by combining hERG (human ether-à-go-go-related gene) channel-drug binding kinetics and multichannel pharmacology. *Circulation: Arrhythm. Electrophysiol.* 10, e004628.
- Macdonald, L.C., Kim, R.Y., Kurata, H., Fedida, D., 2018. Probing the molecular basis of hERG drug block with unnatural amino acids. *Sci. Rep.* 8, 289.
- Mirams, G., Cui, Y., Sher, A., Fink, M., Cooper, J., Heath, B., McMahon, N., Gavaghan, D., Noble, D., 2011. Simulation of multiple ion channel block provides improved early prediction of compounds' clinical torsadogenic risk. *Cardiovasc. Res.* 91 (1), 53–61.
- Nattel, S., Antzelevitch, C., Noble, D., 2011. Resolving the M-cell debate: why and how. *Heart Rhythm* 8, 1293–1295.
- Navarrete, E., Liang, P., Lan, F., Sanchez-Freire, V., Simmons, C., Gong, T., Sharma, A., B. P.W., Patlolla, B., Lee, A., Haodi, W., Beyguy, R., Wu, S., Robbins, R., Beer, D., Wu, J., 2013. Screening drug-induced arrhythmia using human induced pluripotent stem cell-derived cardiomyocytes and low-impedance microelectrode arrays. *Circulation* 128, S3–S13.
- Niederer, S., Kerfoot, E., Benson, A., Bernabeu, M., Bernius, O., Bradley, C., Cherry, E., Clayton, R., Fenton, F., Gurny, A., Heidenreich, E., Land, S., Maleckar, M., Pathmanathan, P., Plank, G., Rodriguez, J.F., Roy, I., Sachse, F., Seemann, G., Skavhaug, O., Smith, N., 1954. Verification of cardiac tissue electrophysiology simulators using an N-version benchmark. *Phil. Trans. Ser. A, Math. Phys. Eng. Sci.* 369, 4331–4351 (2011).
- Nordsletten, D.A., Niederer, S.A., Nash, M.P., Hunter, P.H., Smith, N.P., 2011. Coupling multi-physics models to cardiac mechanics. *Prog. Biophys. Mol. Biol.* 104, 77–88.
- Okada, J., Washio, T., Maehara, A., Momomura, S., Sugiura, S., Hisada, T., 2011. Transmural and apicobasal gradients in repolarization contribute to T-wave genesis in human surface ECG. *Am. J. Physiol. Heart Circ. Physiol.* 301 (1), H200–H208.
- Okada, J., Yoshinaga, T., Kurokawa, J., Washio, T., Furukawa, T., Sawada, K., Sugiura, S., Hisada, T., 2015. Screening system for drug-induced arrhythmic risk combining a patch clamp and heart simulator. *Sci. Adv.* 1 (4) e1400142–e1400142.
- O'Hara, T., Virág, L., Varró, A., Rudy, Y., 2011a. Simulation of the undiseased human cardiac ventricular action potential: model formulation and experimental validation. *PLoS Comput. Biol.* 7 (5), e1002061.
- O'Hara, T., Virág, L., Varró, A., Rudy, Y., 2011b. ORD Orginal Human Ventricular Model. <http://rudylab.wustl.edu/research/cell/code/AllCodes.html>. (Accessed 1 January 2017).
- Parikh, J., Gurev, V., Rice, J., 2017. Novel two-step classifier for torsades de pointes risk stratification from direct features. *Front. Pharmacol.* 8, 818.
- Passini, E., Britton, O.J., Lu, H.R., Rohrbacher, J., Hermans, A.N., Gallacher, D.J., Greig, R.J.H., Bueno-Orovio, A., Rodriguez, B., 2017. Human in silico drug trials demonstrate higher accuracy than animal models in predicting clinical proarrhythmic cardiotoxicity. *Front. Physiol.* 8, 668.
- Pathmanathan, P., Bernabeu, M.O., Bordas, R., Cooper, J., Gurny, A., Pitt-Francis, J.M., Whiteley, D.J., J. P. Gavaghan, 2010. A numerical guide to the solution of the bidomain equations of cardiac electrophysiology. *Prog. Biophys. Mol. Biol.* 102, 136–155.
- Perotti, L., Krishnamoorthi, S., Borgstrom, N., Ennis, D., Klug, W., 2015. Regional segmentation of ventricular models to achieve repolarization dispersion in cardiac electrophysiology modeling. *Int. J. Num. Method. Biomed. Eng.* 28, e02718.
- Perrin, M.J., Subbiah, R.N., Vandenberg, J.I., Hill, A.P., 2008. Human ether-a-go-go related gene HERG K⁺ channels: function and dysfunction. *Prog. Biophys. Mol. Biol.* 98, 137–148.
- Pfizer, 2011. Tikosyn (Dofetilide). NDA 20-931. Risk Evaluation and Mitigation Strategy Document. <https://www.fda.gov/downloads/Drugs/DrugSafety/PostmarketDrugSafetyInformationforPatientsandProviders/UCM266277.pdf>. (Accessed 2 February 2018).
- Priest, J., Gawad, C., Kahlig, K., Yu, J., OHara, T., Boyle, P., Rajamani, S., Clark, M., Garcia, S., Ceresnak, S., Harris, J., Boyle, S., Dewey, F., Malloy-Walton, L., Dunn, K., Grove, M., Perez, M., Neff, N., Chen, R., Maeda, K., Dubin, A., Belardinelli, L., West, J., Antolik, C., Macaya, D., Quertermous, T., Trayanova, N., Quake, S., Ashley, E., 2016. Early somatic mosaicism is a rare cause of long-QT syndrome. *Proc. Natl. Acad. Sci. Unit. States Am.* 113 (41), 115550–11560.
- Qu, Z., Xie, Y., Olcese, R., Karagueuzian, H.S., Chen, P.S., Garfinkel, A., Weiss, J.N., 2013. Early afterdepolarizations in cardiac myocytes: beyond reduced repolarization reserve. *Cardiovasc. Res.* 99, 6–15.
- Redfern, W.S., Carlsson, L., Davis, A.S., Lynch, W.G., MacKenzie, I., Palethorpe, S., Siegl, P.K.S., Strang, I., Sullivan, A.T., Wallis, R., Camm, A.J., Hammond, T.G., 2003. Relationships between preclinical cardiac electrophysiology, clinical QT interval prolongation and torsade de pointes for a broad range of drugs: evidence for a provisional safety margin in drug development. *Cardiovasc. Res.* 58, 32–45.
- Roden, D.M., 2016. Pharmacogenetics of potassium channel blockers. *Cardiac Electrophysiol. Clin.* 8, 385–393.
- Roden, D.M., Lazzara, R., Rosen, M., Schwartz, P.J., Towbin, J., Vincent, G.M., 1996. Multiple mechanisms in the long-QT syndrome. *Circulation* 94, 1996–2012.
- Sadrieh, A., Domanski, L., Pitt-Francis, J., Mann, S., Hodkinson, E.C., Ng, C.A., Perry, M.D., Taylor, J.A., Gavaghan, D., Subbiah, R.N., Vandenberg, J., Hill, A.P., 2014. Multiscale cardiac modelling reveals the origins of notched T waves in long QT syndrome type 2. *Nat. Commun.* 5, 5069.
- Sager, P., Gintant, G., Turner, J., Pettit, S., Stockbridge, N., 2014. Rechanneling the cardiac proarrhythmia safety paradigm: a meeting report from the Cardiac Safety Research Consortium. *Am. Heart J.* 167 (3), 292–300.
- Sahli Costabal, F., Hurtado, D., Kuhl, E., 2016. Generating Purkinje networks in the human heart. *J. Biomech.* 49, 2455–2465.
- Sahli Costabal, F., Hurtado, D., Kuhl, E., 2016. Creating a 3D Fractal Tree on a Given Surface Discretized by Triangles. <https://github.com/fahsli/fractal-tree>. (Accessed 1 January 2017).
- Sahli Costabal, F., Concha, F.A., Hurtado, D.E., Kuhl, E., 2017. The importance of mechano-electrical feedback and inertia in cardiac electromechanics. *Comput. Methods Appl. Mech. Eng.* 320, 352–368.
- Sahli Costabal, F., Yao, J., Kuhl, E., 2018. Predicting drug-induced arrhythmias by multiscale modeling. *Int. J. Numer. Method. Biomed. Eng.* 34 e2964.
- Sahli Costabal, F., Yao, J., Kuhl, E., 2018. Predicting the cardiac toxicity of drugs using a novel multiscale exposure-response simulator. *Comput. Methods Biomed. Eng.* 21, 232–246.
- Sahli Costabal, F., Zaman, J., Kuhl, E., Narayan, S., 2018. Interpreting activation mapping of atrial fibrillation: a hybrid computational/physiological study. *Ann. Biomed. Eng.* 46, 257–269.
- Sato, D., Xie, L.H., Sovari, A.A., Tran, D.X., Morita, N., Xie, F., Karagueuzian, H., Garfinkel, A., Weiss, J.N., Qu, Z., 2009. Synchronization of chaotic early afterdepolarizations in the genesis of cardiac arrhythmias. *Proc. Natl. Acad. Sci. Unit. States Am.* 106, 2983–2988.
- Sher, A.A., Cooling, M.T., Bethwaite, B., Tan, J., Peachey, T., Enticott, C., Garic, S., Gavaghan, D.J., Noble, D., Abramson, D., Crampin, E.J., 2010. A global sensitivity tool for cardiac cell modeling: application to ion current balance and hypertrophic signaling. In: 32nd Annual International Conference of the IEEE EMBS, pp. 1498–1502.

- Sicouri, S., Antzelevitch, C., 1991. A subpopulation of cells with unique electrophysiological properties in the deep subepicardium of the canine ventricle: the M cell. *Circ. Res.* 68, 1729–1741.
- Stewart, P., Aslanidi, O., Noble, D., Noble, P., Boyett, M., Zhang, H., 2009. Mathematical models of the electrical action potential of Purkinje fibre cells. *Phil. Trans.: Math. Phys. Eng. Sci.* 367, 2225–2255.
- Stewart, P., Aslanidi, O.V., Noble, D., Noble, P.J., Boyett, M.R., Zhang, H., 2009. Mathematical Models of the Electrical Action Potential of Purkinje Fibre Cells. <https://models.cellml.org/>. (Accessed 1 January 2017).
- Stockbridge, N., Morganroth, J., Shah, R.R., Garnett, C., 2013. Dealing with global safety issues. *Drug Saf.* 36, 167–182.
- ten Tusscher, K., Noble, D., Noble, P., Panfilov, A., 2004. A model for human ventricular tissue. *Am. J. Physiol. Heart Circ. Physiol.* 286 (4), H1573–H1589.
- Towns, J., Cockerill, T., Dahan, M., Foster, I., Gaither, K., Grimshaw, A., Hazlewood, V., Lathrop, S., Lifka, D., Peterson, G.D., Roskies, R., Scott, J.R., Wilkins-Diehr, N., 2014. Xsede: accelerating scientific discovery. *Comput. Sci. Eng.* 16 (5), 62–74.
- Trudeau, M.C., Warmke, J.W., Ganetzky, B., Robertson, G.A., 1995. HERG, a human inward rectifier in the voltage-gated potassium channel family. *Science* 269, 92–95.
- Vicente, J., Stockbridge, N., Strauss, D.G., 2016. Evolving regulatory paradigm for proarrhythmic risk assessment for new drugs. *J. Electrocardiol.* 49, 837–842.
- Vicente, J., Zusterzeel, R., Johannessen, L., Mason, J., Sager, P., Patel, V., Matta, M.K., Li, Z., Liu, J., Garnett, C., Stockbridge, N., Zineh, I., Strauss, D.G., 2018. Mechanistic model-informed proarrhythmic risk assessment of drugs: review of the “CIPA” initiative and design of a prospective clinical validation study. *Clin. Pharmacol. Ther.* 103, 54–66.
- Wang, W., MacKinnon, R., 2017. Cryo-EM structure of the open human ether-à-go-go-related K⁺ channel hERG. *Cell* 169, 422–430.
- Weiss, N.J., Garfinkel, A., Karagueuzian, H.S., Chen, P.S., Qu, Z., 2010. Early afterdepolarizations and cardiac arrhythmias. *Heart Rhythm* 7, 1891–1899.
- Wong, J., Kuhl, E., 2010. Generating fiber orientation maps in human heart models using Poisson interpolation. *Comput. Methods Biomed. Eng.* 17, 1217–1226.
- Xie, Y., Sato, D., Garfinkel, A., Qu, Z., Weiss, J.N., 2010. So little source, so much sink: requirements for afterdepolarizations to propagate in tissue. *Biophys. J.* 99, 1408–1415.
- Zygote Media Group, 2014. Zygote Solid 3d Heart Generations I & II Development Report. Technical Development of 3D Anatomical Systems.